

A general-purpose single-photon-based quantum computing platform

Nicolas Maring,¹ Andreas Fyrrillas,^{1,*} Mathias Pont,^{1,2,*} Edouard Ivanov,^{1,*} Petr Stepanov,¹ Nico Margaria,¹ William Hease,¹ Anton Pishchagin,¹ Thi Huong Au,¹ Sébastien Boissier,¹ Eric Bertasi,¹ Aurélien Baert,¹ Mario Valdivia,¹ Marie Billard,¹ Ozan Acar,¹ Alexandre Brioussel,¹ Rawad Mezher,¹ Stephen C. Wein,¹ Alexia Salavrakos,¹ Patrick Sinnott,¹ Dario A. Fioretto,² Pierre-Emmanuel Emeriau,¹ Nadia Belabas,² Shane Mansfield,¹ Pascale Senellart,² Jean Senellart,¹ and Niccolo Somaschi¹

¹*Quandela, 7 Rue Léonard de Vinci, 91300 Massy, France*

²*Centre for Nanosciences and Nanotechnologies, CNRS, Université Paris-Saclay, UMR 9001, 10 Boulevard Thomas Gobert, 91120, Palaiseau, France*

(Dated: June 2, 2023)

Quantum computing aims at exploiting quantum phenomena to efficiently perform computations that are unfeasible even for the most powerful classical supercomputers. Among the promising technological approaches, photonic quantum computing offers the advantages of low decoherence, information processing with modest cryogenic requirements, and native integration with classical and quantum networks. To date, quantum computing demonstrations with light have implemented specific tasks with specialized hardware, notably Gaussian Boson Sampling which permitted quantum computational advantage to be reached. Here we report a first user-ready general-purpose quantum computing prototype based on single photons. The device comprises a high-efficiency quantum-dot single-photon source feeding a universal linear optical network on a reconfigurable chip for which hardware errors are compensated by a machine-learned transpilation process. Our full software stack allows remote control of the device to perform computations via logic gates or direct photonic operations. For gate-based computation we benchmark one-, two- and three-qubit gates with state-of-the-art fidelities of $99.6 \pm 0.1\%$, $93.8 \pm 0.6\%$ and $86 \pm 1.2\%$ respectively. We also implement a variational quantum eigensolver, which we use to calculate the energy levels of the hydrogen molecule with high accuracy. For photon native computation, we implement a classifier algorithm using a 3-photon-based quantum neural network and report a first 6-photon Boson Sampling demonstration on a universal reconfigurable integrated circuit. Finally, we report on a first heralded 3-photon entanglement generation, a key milestone toward measurement-based quantum computing.

Realizations of quantum computing (QC) have built on rapid progress in controlling physical systems that can support quantum information such as superconducting circuits (e.g. [1, 2]), trapped ions (e.g. [3, 4]), neutral atoms (e.g. [5]) and light (e.g. [6, 7]). These technological breakthroughs have brought four platforms to the regime of quantum computational advantage [1, 2, 8–10], by solving specific sampling problems that would require unreasonable computing time even for the most powerful classical supercomputers. Two of these four are photonic, highlighting the position of light-based technology among the leading platforms. Quantum light as quantum information carrier offers the advantage of low decoherence and comes with a large choice of degrees of freedom to encode the information, while providing natural connectivity for distributed or blind quantum computing [11].

Over the years, a variety of proposals for universal fault-tolerant computing have been put forward in the discrete-variable photonic approach in which quantum information is encoded with single photons [12–16]. With identified thresholds, these roadmaps motivate the development of quantum computing hardware based on single-photon sources, integrated photonic chips and single-photon detectors. Experimental progress of ever increas-

ing complexity has been achieved with integrated sources exploiting nonlinear effects, including with large-scale integrated chips [17, 18]. However, the probabilistic nature of the single-photon generation process, the need for it to be heralded and the requirement to operate at low efficiency to limit multiphoton events are strong constraints on the hardware architecture. This has resulted in a limited number of manipulated photons with typical rates in the mHz range for 4 photons and the demonstration of specific information processing tasks relying on dedicated photonic chips [18]. Overcoming these limitations is foreseen through the use of massive multiplexing of hundreds of heralded sources [19].

Another path to large-scale QC with single photons has progressively emerged owing to deterministic single photon source devices based on semiconductor quantum dots (QDs) [20–24]. Such sources have demonstrated record single-photon generation efficiency, 10-20 times higher than their nonlinear counterparts, allowing for a drastic reduction in resource requirements. Such efficiencies allowed a record manipulation of 14 single photons in a free-space Boson Sampling experiment [25]. Very recently, the same QD sources have shown their ability to deterministically generate photonic cluster states at high rate [26], reducing even further the foreseen overheads for large-scale measurement-based quantum computation [27].

* These authors contributed equally to this work.

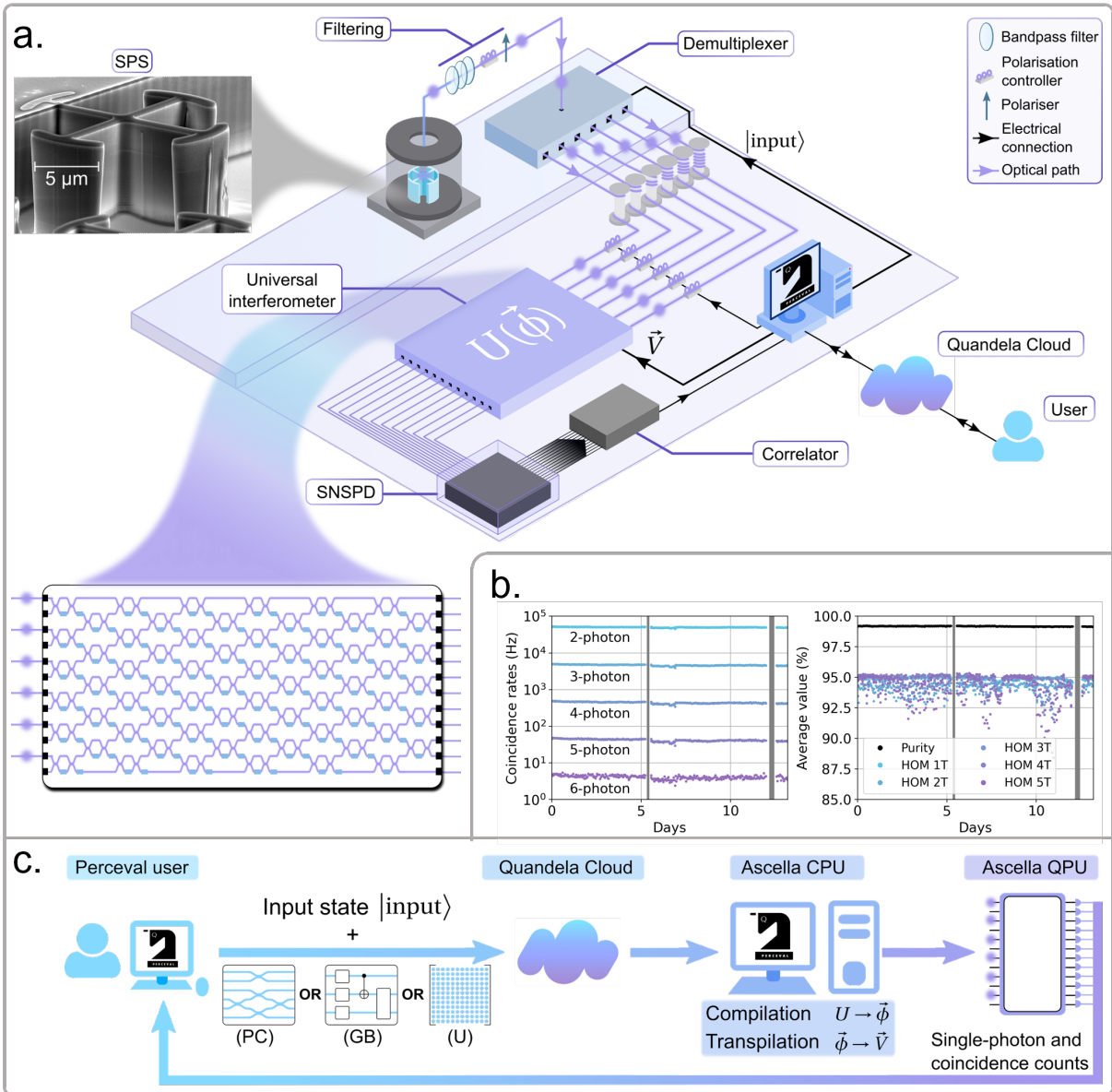


FIG. 1: Architecture, performance and stability of Ascella. **a.** Sketch of the overall architecture of the 6 single-photon quantum computer. A quantum-dot single-photon source (SPS) device at 5K is operated at 80 MHz repetition rate. An active demultiplexer followed by fibered delays converts the train of single photons into 6 photons arriving simultaneously to the universal 12-mode photonic chip. Photons are detected at the chip output by superconducting nanowire single-photon detectors (SNSPD) and detection times are processed by a correlator. A full software stack controls the unitary matrix U implemented on the chip through the voltages \vec{V} applied on 126 thermal phase shifters, yielding phase shifts $\vec{\phi}$, and the photonic input state according to the job requested. It also recalibrates hourly and readjusts all hardware control knobs for optimal performance. The single photons are sent into a photonic chip featuring a universal interferometer scheme capable of implementing any 12×12 unitary matrix. **b.** Detected N -photon coincidence rates for N -photon inputs as a function of time, with the photonic circuit configured to implement the identity matrix. Rates are integrated for 50 seconds. Grey areas correspond to maintenance and upgrade periods. In right figure, we also monitor the on-chip photon indistinguishability and single-photon purity quantified respectively by the Hong-Ou-Mandel (HOM) visibility V_{HOM} and $1 - g^{(2)}(0)$, where $g^{(2)}$ is the normalized second-order correlation function. HOM kT is V_{HOM} for delays $k \times \Delta T$ between emitted photons where $\Delta T = 180$ ns. Each data point corresponds to a correlation histogram integrated over 10 seconds. **c.** Job execution flowchart on Ascella. *Perceval* users may send jobs consisting in photonic circuits (PC), or a gate-based circuit (GB), or a unitary matrix (U), along with the desired input state to the Quandela Cloud. The job is first processed by a CPU, which computes the necessary phase shifts $\vec{\phi}$ to apply, and subsequently the voltages \vec{V} for the on-chip phase shifters from our compilation and transpilation process. Finally, the user receives the collected single-photon and coincidence counts after the computation on the quantum processing unit (QPU).

In the present work, we report on the first general-purpose user-ready single-photon-based quantum computing machine, named Ascella. It is cloud-accessible [28] and based on six photonic qubits generated by an on-demand QD source. The quantum information is encoded in the path degree of freedom and arbitrarily manipulated in a 12-mode integrated universal interferometer. A machine-learned transpilation process corrects for the hardware manufacturing errors. Ascella operates the largest number of single photons on chip to date with a 6-photon sampling rate of 4 Hz and shows operation stability over weeks. We benchmark its performances and demonstrate applications both in the gate-based and photonic computation frameworks. Each reported result represents either state-of-the-art performance or first-ever experimental demonstration for which we provide the full code to reproduce through Quandela Cloud. The numerous applications illustrate the general-purpose potential of the machine for noisy near-term quantum computing. We finally discuss the evolution of the reported platform towards scale-up, and demonstrate for the first time a critical step for future measurement-based quantum computation: heralded entanglement generation of three-photon GHZ states.

SINGLE-PHOTON BASED COMPUTER

Architecture

Ascella’s hardware, as shown in Fig. 1.a, comprises an on-demand high-brightness single-photon source, a programmable optical demultiplexer allowing up to 6 single photons to simultaneously interfere on a 12-mode reconfigurable universal interferometer, and a single-photon detection and post-processing unit.

The on-demand single-photon source (see Supplementary S-I) based on an InGaAs quantum dot in a microcavity [20] is optically excited at an 80 MHz rate. It exploits a neutral dot and LA-phonon-assisted near-resonant excitation [29] to emit linearly-polarized single photons with 55% probability into the collection lens. To send 6 single photons to every even input mode of the chip, an active optical demultiplexer sequentially deflects the photon stream into 6 optical fibers of different lengths adjusted to synchronize the photons [30]. Using optical shutters, the demultiplexer can prepare any input state from $|000000000000\rangle$ to $|101010101010\rangle$ (photon positions can subsequently be swapped, see Supplementary S-II). The 12-mode photonic integrated circuit (Si_3N_4 platform) is composed of 126 voltage-controlled thermo-optic phase shifters and 132 directional couplers [31] which are laid out in a rectangular universal interferometer scheme (see Fig.1.a). Finally, the 12 outputs of the circuit are connected to high-efficiency superconducting nanowire single-photon detectors (SNSPD), and N -photon detection events are registered using a time-to-digital converter.

The average total efficiency of the optical setup is $\sim 8\%$, including the single-photon source device brightness, transmission of all optical components, and detection efficiencies (see Supplementary S-II). This leads to record-breaking 2- to 4-photon on-chip coincidence rates (Fig. 1.b) and the first on-chip processing of 5 and 6 photons, at respective rates of 50 Hz and 4 Hz. We measure high single-photon purity $> 99\%$, high indistinguishability $\sim 94\%$ independent of the delays between photon emission (up to $1\ \mu\text{s}$), resulting in a measured on-chip 2-photon interference visibility for all 15 pairs of $91 - 94\%$ (see Supplementary S-III). The genuine 4- and 6-photon indistinguishability defined as the probability that the N photons are identical establishes a new record value of 0.85 ± 0.02 for 4 photons [32], and a first study for 6 photons with value of 0.76 ± 0.02 . We ensure long-term stability and high-performance operation of Ascella by monitoring key metrics and by carrying out automated hourly system optimization runs. This guarantees a highly-stable and long-term operation over several weeks (see Fig.1.b), robust against external temperature fluctuations and mechanical perturbations.

To operate the machine, tasks are sent remotely with the python-based open-source framework *Perceval* [33]. The user can either specify (see Fig.1.c) a photonic circuit (PC), a gate-based circuit (GB) or a unitary transformation (U) to be applied to a specified input state containing 1 to 6 photons, and optional postselection criteria. Output photon coincidences are then acquired up to the desired sample number and data sample results are sent back to the user either as a stream of events or as an aggregated `state:count` inventory.

Chip control

The rectangular universal interferometer layout (see Fig. 1.a) is ideally based on balanced directional couplers (i.e. 50% reflectivity). Experimentally, we observe reflectivities with average values of $(56.7 \pm 0.6)\%$ for our chip at the operation wavelength of 928 nm. The systematic error stemming from the fabrication process and wavelength dependency. These errors reduce the range of implementable 12×12 unitary matrices [34, 35] and, if not compensated for, affect the fidelity of the implemented unitary matrix to the target unitary matrix. To address these limitations, we designed a custom compilation and transpilation process that converts with high fidelity user-provided photonic circuits, unitary matrices or gate-based circuits into interferometer phase shift values (compilation) then into voltages to apply on the chip phase shifters (transpilation). Initially, a global optimization step fine-tunes the phase shifts to enhance matrix fidelity. Subsequently, the process calculates the voltages to apply on the chip phase shifters while compensating for thermal crosstalk. The thermo-optic phase shifters can be modelled by $\vec{\phi} = A\vec{V}^{\odot 2} + \vec{b}$ where the vector $\vec{\phi}$ contains all 126

physical phase shifts, \vec{V} the 126 applied voltages and \odot^2 represents element-wise squaring. Off-diagonal elements of the 126×126 matrix A represent thermal crosstalk between phase shifters. We engineered a machine learning-based process that optimizes the values of A and \vec{b} , constituting more than 16000 free parameters to determine. The same process also estimates individual directional coupler reflectivities and relative output losses (see Supplementary S-IV for values). This process offers a 7-fold improvement on the transpilation ($\vec{\phi}$ to \vec{V} process) over more standard characterization techniques involving interference-fringe measurements (see Methods). The full compilation and transpilation processes achieve an average fidelity of $F = 99.7 \pm 0.08$ following the fidelity evaluation procedure from Ref. [31].

GATE-BASED QUANTUM COMPUTATION

Following the KLM scheme [36], Ascella can perform probabilistic gate-based protocols. Within this quantum computation framework, we benchmark quantum logic gates on up to three qubits and implement a hybrid variational quantum eigensolver.

Benchmarking logic gates

Ideally, a gate U applied to an initial pure state $|\psi\rangle$ will produce the pure state $U|\psi\rangle$. In reality, errors, quantified by a noise channel Λ [37], corrupt the final state, which is then described by a density matrix $\rho = \Lambda(U|\psi\rangle\langle\psi|U^\dagger)$. A standard figure of merit to quantify the gate performance is the quantum state fidelity $F_\psi(U) = \langle\psi|U^\dagger\rho U|\psi\rangle$ of the final state ρ to the ideal state $U|\psi\rangle$. To assess Ascella's performance for a given gate, we evaluate the fidelity of the gate averaged over all possible input states $|\psi\rangle$, i.e. $F_{\text{avg}}(U) = \int F_\psi(U)d\psi$, where the integral is taken over the Haar measure [38].

A brute-force approach to estimating $F_{\text{avg}}(U)$ requires an impractically large number of measurements. A more efficient method, randomized benchmarking, has been proposed for matter qubits [39] but applies long sequences of gates from specific sets of unitaries [40]. Since photonic quantum processing converts any quantum circuit to a photonic circuit [41], we use a new method to evaluate F_{avg} [42]. Our method exploits symmetries so that the contribution of most F_ψ s to F_{avg} cancel out, allowing F_{avg} to be expressed as a finite discrete sum $F_{\text{avg}} = \sum_{i=1}^K w_i m_i$ of K expectation values m_i with weight w_i (see Supplementary S-V). The w_i and the state preparation and measurement configurations for each m_i depend on the gate U and are pre-computed. Each configuration consists in preparing an unentangled initial state $|\psi\rangle$, applying the gate and performing single-qubit Pauli measurements. For the gates benchmarked on As-

Qubits, n	Gate, U	$F_{\text{avg}}(U)$ (%)	M	K	2^{4n}
1	T -gate	99.6 ± 0.1	4	4	16
2	CNOT	93.8 ± 0.6	36	58	256
3	Toffoli	86 ± 1.2	340	593	4096

TABLE I: Average gate fidelities of 1-, 2- and 3-qubit gates implemented by Ascella evaluated based on K expectation values obtained from M measurement configurations.

cella (see Table I), the K expectation values m_i are obtained from $M \leq K$ measurement configurations, with K less than the $\sim 2^{4n}$ measurements required for full process tomography [43] of an n -qubit gate.

The average gate fidelities measured for a T -gate defined as $T := |0\rangle\langle 0| + e^{i\frac{\pi}{4}}|1\rangle\langle 1|$ [44], a CNOT gate, and a Toffoli gate are shown in Table I. These measurements set a first benchmark for universal photonic quantum computing and are on par with the benchmarked performance of open-access quantum computing platforms based on ions and superconducting qubits (see Supplementary S-V). These values are a lower bound on the true average gate fidelities since they also include errors related to state preparation and measurement (SPAM) roughly given by $(1 - F_{\text{avg}}(T\text{-gate})^{2n/3})$, which is $0.3 \pm 0.1\%$ for the T -gate, $0.5 \pm 0.1\%$ for the CNOT gate, and $0.8 \pm 0.2\%$ for the Toffoli gate.

Variational quantum eigensolver

We illustrate gate-based computation possibilities by implementing a variational quantum eigensolver (VQE) algorithm to compute the ground state energies of an H_2 molecule. VQE exploits the variational principle stating that given a Hamiltonian $\hat{\mathcal{H}}$ and an ansatz wavefunction $|\psi(\vec{\theta})\rangle$ parameterized by $\vec{\theta}$, the ground state energy associated with $\hat{\mathcal{H}}$ satisfies $E_0 \leq \langle\psi(\vec{\theta})|\hat{\mathcal{H}}|\psi(\vec{\theta})\rangle$ [45, 46]. In this context, VQE explores the state space by minimizing the energy to find a good approximation of E_0 .

We build the fermionic Hamiltonian for H_2 using the symmetry-conserving Bravyi-Kitaev transformation [47], which is available through the *OpenFermion* [48] python package (details are given in Methods). Symmetry allows reduction of the problem to the effective Hamiltonian $\hat{\mathcal{H}}_{\text{qubit}}$ which acts on two qubits expressed in the standard Pauli basis (\mathbb{I} , X , Y , and Z),

$$\hat{\mathcal{H}}_{\text{qubit}} = \alpha\mathbb{I}\mathbb{I} + \beta Z\mathbb{I} + \gamma\mathbb{I}Z + \delta ZZ + \mu XX \quad (1)$$

with real parameters α , β , γ , δ and μ that depend on the choice of bond length. We create ansatz states $|\psi(\vec{\theta})\rangle$ made of two path-encoded qubits using single-qubit operations $R(\vec{\theta}_i)$ and an entangling postselected CNOT gate (see Fig. 2.a). The expectation value of $\hat{\mathcal{H}}_{\text{qubit}}$ on $|\psi(\vec{\theta})\rangle$ is obtained from the weighted averages of 10000 post-processed 2-photon samples. The classical processor then

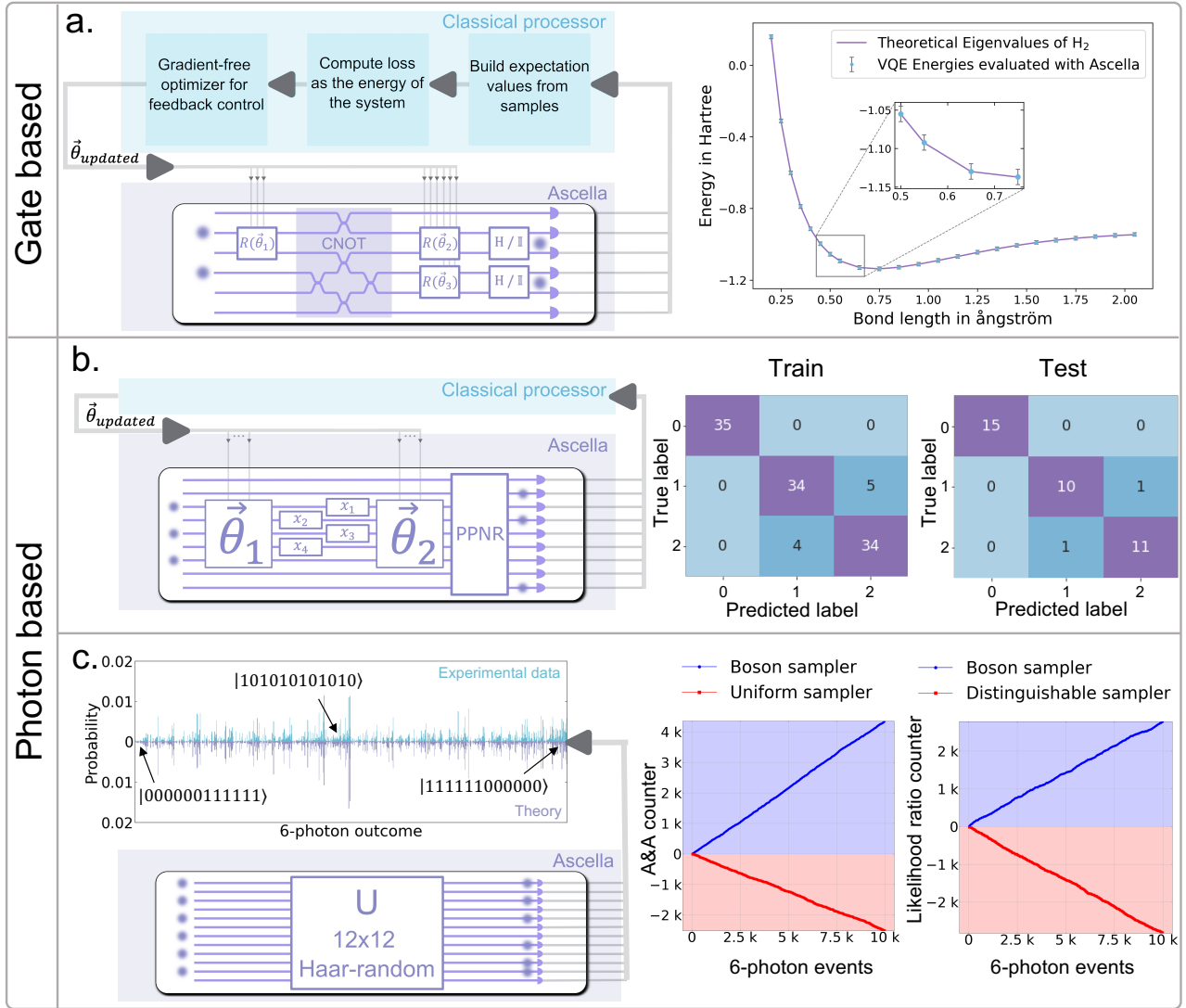


FIG. 2: **a. Gate-based computation.** Hybrid variational quantum eigensolver. On Ascella, the single-qubit gates $R(\vec{\theta}_i)$, together with a CNOT gate, create an ansatz 2-qubit state. We then measure in the Z basis (using the identity gate \mathbb{I}) or in the X basis (using the Hadamard gate H). The output counts (grey arrow) are sent to a classical processor which reconstructs the corresponding energy and implements a feedback loop to update the single-qubit gate angles $\vec{\theta}_i$ via a gradient-free optimizer and find an ansatz closer to the ground state. Each iteration on the QPU takes about 22 s (including 14 s of QPU time and classical communication to the cloud). The error bars are computed assuming a shot-noise limited error on the 2-photon coincidences. **b.-c. Photon-native computation.** **b.** Classification task using a quantum neural network. Confusion matrices for the classification of the IRIS dataset on Ascella: training dataset (left), test dataset (right). The accuracy is 0.92 for the training set and 0.95 for the test set. **c.** 6 single-photon Boson Sampling. Measured (top) and modelled (bottom) 6-photon output distributions for the input state $|1010101010\rangle$. The 924 6-photon outcomes are canonically ordered from $|000000111111\rangle$ to $|111111000000\rangle$. Discrimination between Boson Sampling and uniform sampling hypothesis using the Aaronson and Arkhipov (A & A) counter and between Boson Sampling and distinguishable sampling hypothesis using the likelihood ratio counter. The value of each discriminator is updated every 10^9 samples, which corresponds to ~ 20 6-photon events. In both cases, a positive slope validates the test (see Methods).

evaluates a loss function using a gradient-free optimizer based on expectation values obtained from Ascella and corrected with an error mitigation scheme inspired by Ref. [49]. Then $\vec{\theta}$ is updated classically in a feedback

loop between Ascella and a classical processor to reach lower and lower energies. Error mitigation helps to consistently reach the ground state energy (see Supplementary S-VIII). For any initial random parameters and bond

length, the algorithm consistently converges to the theoretical eigenvalue within ± 0.01 Hartree in 50 to 100 iterations (see Fig. 2.a). The total experiment time per bond length is approximately four times faster than previous photonic VQE experiments of a system with the same number of degrees of freedom [45]. In an experiment with fixed initial conditions and bond length, chemical accuracy (an error of ± 0.0016 Hartree) was achieved with a success probability of 93%, showing greater accuracy than recent photonic VQE experiments [49]. These two improvements are due to higher quality single-photon sources and chip control.

PHOTON-NATIVE QUANTUM COMPUTATION

We now demonstrate the operation of Ascella in its native photonic framework, where the information is directly processed through photonic quantum interferences in an arbitrary unitary transformation and detection.

Photon-based quantum neural network

We train a quantum neural network [50] on Ascella for a supervised learning classification task. We build a variational quantum algorithm where, taking inspiration from Ref. [51], we use a native photonic ansatz. We perform multi-class classification on the well-known IRIS dataset [52]. To the best of our knowledge, this is the first experimental implementation of a variational quantum classifier with single photons – we refer to Ref. [53] for a realization on a superconducting platform and to Ref. [54] for a 2-photon classifier based on kernel methods. Following our photon-native approach, we design the ansatz of the variational algorithm directly using the beamsplitters and phase shifters on 5 modes of Ascella, in which we input 3 photons. We also implement partial pseudo photon-number resolution by exploiting 4 extra modes of the chip.

We train the model using a see-saw optimization between the chip parameters and the output state parameters that define the measurement observable. Each iteration requires 112 experiments, one for each data point in the training set, and we gather 50000 samples per run. A batch functionality in *Perceval* [33] allows us to send all data points as one job to the server. Details on the ansatz and the training can be found in Methods and Supplementary S-VII. After about 15 iterations, we find an accuracy of 0.92 on the training set and 0.95 on the test set. Fig. 2.b. provides a summary of the model predictions versus actual labels as a confusion matrix.

Boson Sampling with 6 single photons

Boson Sampling is a sampling problem suited for demonstrating a quantum-over-classical advantage with

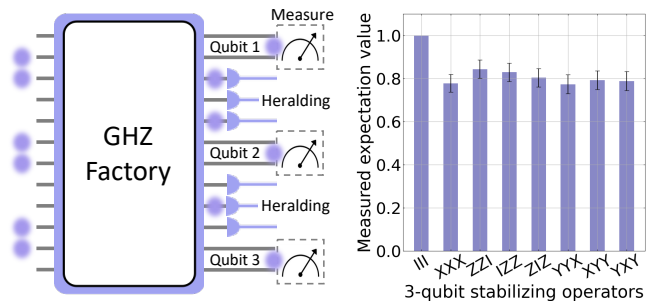


FIG. 3: **Heralded generation of 3-photon GHZ states.** Measured expectation values of the stabilizing operators of the heralded 3-photon GHZ state $|\text{GHZ}_3^+\rangle$ yielding a fidelity of $F_{\text{GHZ}_3^+} = 0.82 \pm 0.04$.

optical quantum computing platforms [55]. The recent demonstrations of quantum advantage [6, 10] in the Gaussian Boson Sampling framework [56] used squeezed light manipulated in free-space interferometers to limit optical losses. Genuine single-photon-based Boson Sampling has progressed poorly on integrated chips due to the low efficiency of heralded sources [57–60]. Here we demonstrate on-chip Boson Sampling for a record number of 6 photons with a fully reconfigurable interferometer. A 12×12 Haar-random unitary matrix is randomly chosen using the dedicated tool in *Perceval*. We record the threshold statistics of all N -photon coincidences ($N \in \llbracket 1; 6 \rrbracket$) and acquire in total 340.10^9 samples, with a 6-photon coincidence rate reduced by the strong bunching of photons in this sampling task down to 0.16 Hz.

To validate our experimental results, we discriminate our collected Boson Sampling statistics from the uniform sampler [61] and distinguishable sampler [62] hypotheses (see Fig. 2.c). We also reconstruct the 6-photon output distribution from the sampled data and compare it to the ideal output distribution corresponding to the chosen unitary matrix. Both distributions are plotted in Fig. 2.c from which we deduce a fidelity $F = \sum_i \sqrt{p_i q_i}$ and a total variation distance $D = \frac{1}{2} \sum_i |p_i - q_i|$ where $\{p_i\}$ and $\{q_i\}$ are the ideal and experimental output probability distributions respectively, with $i \in \{1, \dots, 924\}$ labelling the no-collision output configuration of the boson-sampling device [55]. We measure state-of-the-art values $F = (0.97 \pm 0.03)$ and $D = (0.16 \pm 0.02)$ [25, 63]. Details about the measurement simulation with *Perceval* as well as Boson Sampling with k photons lost ($k \in \llbracket 1; 4 \rrbracket$) are given in Supplementary S-VI.

DISCUSSION AND RESOURCES TO SCALE UP

The above results demonstrate the suitability of the architecture for near-term quantum computing tasks. The record 4 Hz rate for 6 photons demonstrated here can further be pushed by optimizing each individual com-

ponent of the platform. This optimization will allow manipulating a large number of photons in a reasonable time (see Supplementary S-II). Noticeably, the current single-photon source efficiency of 55% at the first lens can be brought to values at least as high as 96% with technology optimization [64]. In parallel, the number of modes in the photonic chip can be increased, the photonic chip side, a record number of 32 modes was recently reported with a high-transmission glass chip technology [60] and progress is continually achieved with silicon nitride-based platforms [17, 18]. Our single-photon source technology has demonstrated $\geq 99.5\%$ indistinguishability [20], which would bring the two-qubit gates fidelity close to unity [65]. These improvements will allow linear-optical computing platforms to push to dozens of photons. Scaling-up beyond the limitations of probabilistic linear-optical protocols involves shifting to a measurement-based quantum computing paradigm, which requires the generation of large graph states [12]. A key step to obtain large graph states is the heralded-generation of entanglement on chip [13]. This is the last feature we implement on Ascella, demonstrating for the first time the heralded generation of 3-photon GHZ states from a 6-photon input state.

We use a scheme adapted from Ref. [13, 66] where 3 out of the 6 single photons are detected in 6 optical modes identified as 8 heralding states (see Methods). Four of them herald the generation of the state $|\text{GHZ}_3^+\rangle = (|000\rangle + |111\rangle)/\sqrt{2}$. The fidelity of the heralded state to the target state is characterized on Ascella using $F_{\text{GHZ}_3^+} = \frac{1}{8} \sum_i \langle S_i \rangle$, where $S_i \in \{III, XXX, ZZI, IZZ, ZIZ, -YYX, -XYY, -YXY\}$ are the stabilizing operators of the target state and are experimentally accessed through the 3-qubit operators XXX , ZZZ , YYX , XYY , and YXY . All expectation values $\langle S_i \rangle$ are reported in Fig. 3, and yield a fidelity of $F_{\text{GHZ}_3^+} = 0.82 \pm 0.04$ (see Methods) providing the first benchmarking of such heralded state generation.

Such heralded entanglement schemes combined with the recent demonstration of efficient generation of linear cluster states directly from the same quantum dot source technology [26] open the path to fault tolerant quantum computing with reasonable hardware resource overheads.

ACKNOWLEDGEMENTS

The authors would like to thank A. White for fruitful feedback, R. Osellame and his team for valuable interactions on the generation of heralded GHZ states, JJ.

Dormard, G. Parent, J. Herlent for support in the electronic modules. The authors acknowledge I. Maillette de Buy Wenniger, V. Guichard, F. Hoch, and A. Henry for preliminary work on the classification experiment. This work has received funding from the European Union’s Horizon 2020 Research and Innovation Programme QUDOT-TECH under the Marie Skłodowska Curie Grant Agreement No. 861097, and from BPI France Concours Innovation PIA3 projects DOS0148634/00 and DOS0148633/00 – Reconfigurable Optical Quantum Computing.

AUTHOR CONTRIBUTIONS

Correspondance should be addressed to J. Senellart (jean.senellart@quandela.com) and N. Somaschi (niccolo.somaschi@quandela.com).

The QD single photon source was fabricated by A.P., N. Marg., W.H., S.B. and H.A.; its optical characterization was performed by P. St.; A.F., E.I., M.P., M.B., O.A. and A.B. integrated all the hardware components under the close supervision of N.M.; A.F., N.M., N.B. and J.S. developed the machine-learned chip control; E.I., A.F. and M.P. developed the software layer controlling all instruments and realizing the remote tasks; M.V. architected the software stack, E.B. implemented the control code within *Perceval* and A.B. wrote the interface between *Perceval* and the cloud worker; R.M., S.W. P.Si. and J.S. conducted the gate benchmarking; M.P. and R.M. ran the Boson Sampling task; M.P. implemented the 6-photon indistinguishability test and heralded 3-photon GHZ state generation; A.S. and D.F. realized the classification experiment, P.Si. and P-E.E. defined and realized the VQE; S.M. supervised and coordinated the theoretical work; P.Se. and N.S. guided the source fabrication process and hardware integration; J.S. coordinated the full assembly of the hardware and software; N.S. supervised the overall project; M.P., P-E.E., A.S., R.M., N.M., P.Si., A.F., S.W., N.S., N.B, S.M., J.S., P.Se. wrote the paper.

DATA & CODE AVAILABILITY

The data generated as part of this work is available upon reasonable request from the corresponding authors. The code used to run the presented applications is available at <https://github.com/Quandela/Ascella>.

[1] Frank Arute, Kunal Arya, Ryan Babbush, Dave Bacon, Joseph C Bardin, Rami Barends, Rupak Biswas, Sergio Boixo, Fernando GSL Brandao, David A Buell, et al. Quantum supremacy using a programmable supercon-

ducting processor. *Nature*, 574(7779):505–510, 2019.

[2] Qingling Zhu, Sirui Cao, Fusheng Chen, Ming-Cheng Chen, Xiawei Chen, Tung-Hsun Chung, Hui Deng, Yajie Du, Daojin Fan, Ming Gong, et al. Quantum compu-

- tational advantage via 60-qubit 24-cycle random circuit sampling. *Science bulletin*, 67(3):240–245, 2022.
- [3] SA Moses, CH Baldwin, MS Allman, R Ancona, L Ascarrunz, C Barnes, J Bartolotta, B Bjork, P Blanchard, M Bohn, et al. A race track trapped-ion quantum processor. *arXiv preprint arXiv:2305.03828*, 2023.
- [4] Shantanu Debnath, Norbert M Linke, Caroline Figgatt, Kevin A Landsman, Kevin Wright, and Christopher Monroe. Demonstration of a small programmable quantum computer with atomic qubits. *Nature*, 536(7614): 63–66, 2016.
- [5] Dolev Bluvstein, Harry Levine, Giulia Semeghini, Tout T Wang, Sepehr Ebadi, Marcin Kalinowski, Alexander Keesling, Nishad Maskara, Hannes Pichler, Markus Greiner, et al. A quantum processor based on coherent transport of entangled atom arrays. *Nature*, 604(7906): 451–456, 2022.
- [6] Han-Sen Zhong, Yu-Hao Deng, Jian Qin, Hui Wang, Ming-Cheng Chen, Li-Chao Peng, Yi-Han Luo, Dian Wu, Si-Qiu Gong, Hao Su, et al. Phase-programmable gaussian boson sampling using stimulated squeezed light. *Physical review letters*, 127(18):180502, 2021.
- [7] Juan M Arrazola, Ville Bergholm, Kamil Brádler, Thomas R Bromley, Matt J Collins, Ish Dhand, Alberto Fumagalli, Thomas Gerrits, Andrey Goussev, Lukas G Helt, et al. Quantum circuits with many photons on a programmable nanophotonic chip. *Nature*, 591(7848): 54–60, 2021.
- [8] Yulin Wu, Wan-Su Bao, Sirui Cao, Fusheng Chen, Ming-Cheng Chen, Xiawei Chen, Tung-Hsun Chung, Hui Deng, Yajie Du, Daojin Fan, et al. Strong quantum computational advantage using a superconducting quantum processor. *Physical review letters*, 127(18):180501, 2021.
- [9] Lars S Madsen, Fabian Laudenbach, Mohsen Falamarzi Askarani, Fabien Rortais, Trevor Vincent, Jacob FF Bulmer, Filippo M Miatto, Leonhard Neuhaus, Lukas G Helt, Matthew J Collins, et al. Quantum computational advantage with a programmable photonic processor. *Nature*, 606(7912):75–81, 2022.
- [10] Han-Sen Zhong, Hui Wang, Yu-Hao Deng, Ming-Cheng Chen, Li-Chao Peng, Yi-Han Luo, Jian Qin, Dian Wu, Xing Ding, Yi Hu, et al. Quantum computational advantage using photons. *Science*, 370(6523):1460–1463, 2020.
- [11] Anne Broadbent, Joseph Fitzsimons, and Elham Kashefi. Universal blind quantum computation. *2009 50th Annual IEEE Symposium on Foundations of Computer Science*, pages 517–526, 2009.
- [12] Robert Raussendorf and Hans J Briegel. A one-way quantum computer. *Physical review letters*, 86(22):5188, 2001.
- [13] Ying Li, Peter C Humphreys, Gabriel J Mendoza, and Simon C Benjamin. Resource costs for fault-tolerant linear optical quantum computing. *Physical Review X*, 5(4):041007, 2015.
- [14] Daniel Herr, Alexandru Paler, Simon J Devitt, and Franco Nori. A local and scalable lattice renormalization method for ballistic quantum computation. *npj Quantum Information*, 4(1):27, 2018.
- [15] James M Auger, Hussain Anwar, Mercedes Gimeno-Segovia, Thomas M Stace, and Dan E Browne. Fault-tolerant quantum computation with nondeterministic entangling gates. *Physical Review A*, 97(3):030301, 2018.
- [16] Sara Bartolucci, Patrick Birchall, Hector Bombin, Hugo Cable, Chris Dawson, Mercedes Gimeno-Segovia, Eric Johnston, Konrad Kieling, Naomi Nickerson, Mihir Pant, et al. Fusion-based quantum computation. *Nature Communications*, 14(1):912, 2023.
- [17] Caterina Vigliar, Stefano Paesani, Yunhong Ding, Jeremy C Adcock, Jianwei Wang, Sam Morley-Short, Davide Bacco, Leif K Oxenløwe, Mark G Thompson, John G Rarity, et al. Error-protected qubits in a silicon photonic chip. *Nature Physics*, 17(10):1137–1143, 2021.
- [18] Jueming Bao, Zhaorong Fu, Tanumoy Pramanik, Jun Mao, Yulin Chi, Yingkang Cao, Chonghao Zhai, Yifei Mao, Tianxiang Dai, Xiaojiong Chen, et al. Very-large-scale integrated quantum graph photonics. *Nature Photonics*, pages 1–9, 2023.
- [19] Hector Bombin, Isaac H Kim, Daniel Litinski, Naomi Nickerson, Mihir Pant, Fernando Pastawski, Sam Roberts, and Terry Rudolph. Interleaving: Modular architectures for fault-tolerant photonic quantum computing. *arXiv preprint arXiv:2103.08612*, 2021.
- [20] Niccolo Somaschi, Valerian Giesz, Lorenzo De Santis, JC Laredo, Marcelo P Almeida, Gaston Hornecker, S Luca Portalupi, Thomas Grange, Carlos Anton, Justin Demory, et al. Near-optimal single-photon sources in the solid state. *Nature Photonics*, 10(5):340–345, 2016.
- [21] Xing Ding, Yu He, Z-C Duan, Niels Gregersen, M-C Chen, S Unsleber, Sebastian Maier, Christian Schneider, Martin Kamp, Sven Höfling, et al. On-demand single photons with high extraction efficiency and near-unity indistinguishability from a resonantly driven quantum dot in a micropillar. *Physical review letters*, 116(2):020401, 2016.
- [22] Hui Wang, Yu-Ming He, T-H Chung, Hai Hu, Ying Yu, Si Chen, Xing Ding, M-C Chen, Jian Qin, Xiaoxia Yang, et al. Towards optimal single-photon sources from polarized microcavities. *Nature Photonics*, 13(11):770–775, 2019.
- [23] Ravitej Uppu, Freja T Pedersen, Ying Wang, Cecilie T Olesen, Camille Papon, Xiaoyan Zhou, Leonardo Midolo, Sven Scholz, Andreas D Wieck, Arne Ludwig, et al. Scalable integrated single-photon source. *Science advances*, 6(50):eabc8268, 2020.
- [24] Natasha Tomm, Alisa Javadi, Nadia Olympia Antoniadis, Daniel Najer, Matthias Christian Löbl, Alexander Rolf Korsch, Rüdiger Schott, Sascha René Valentin, Andreas Dirk Wieck, Arne Ludwig, et al. A bright and fast source of coherent single photons. *Nature Nanotechnology*, 16(4):399–403, 2021.
- [25] Hui Wang, Jian Qin, Xing Ding, Ming-Cheng Chen, Si Chen, Xiang You, Yu-Ming He, Xiao Jiang, L You, Z Wang, et al. Boson sampling with 20 input photons and a 60-mode interferometer in a 1 0 14-dimensional hilbert space. *Physical review letters*, 123(25):250503, 2019.
- [26] N Coste, D Fioretto, N Belabas, SC Wein, P Hilaire, R Frantzeskakis, M Gundin, B Goes, N Somaschi, M Morassi, et al. High-rate entanglement between a semiconductor spin and indistinguishable photons. *arXiv preprint arXiv:2207.09881*, 2022.
- [27] Mercedes Gimeno-Segovia, Pete Shadbolt, Dan E Browne, and Terry Rudolph. From three-photon greenberger-horne-zeilinger states to ballistic universal quantum computation. *Physical review letters*, 115(2): 020502, 2015.
- [28] Quandela. Quandela cloud, 2022. <https://cloud.quandela.com>.

- [29] SE Thomas, M Billard, N Coste, SC Wein, H Ollivier, O Krebs, L Tazaïrt, A Harouri, A Lemaitre, I Sagnes, et al. Bright polarized single-photon source based on a linear dipole. *Physical review letters*, 126(23):233601, 2021.
- [30] Mathias Pont, Giacomo Corrielli, Andreas Fyrrillas, Iris Agresti, Gonzalo Carvacho, Nicolas Maring, Pierre-Emmanuel Emeriau, Francesco Ceccarelli, Ricardo Albiero, Paulo HD Ferreira, et al. High-fidelity generation of four-photon ghz states on-chip. *arXiv preprint arXiv:2211.15626*, 2022.
- [31] Caterina Taballione, Reinier van der Meer, Henk J Snijders, Peter Hooijschuur, Jörn P Epping, Michiel de Goede, Ben Kassenberg, Pim Venderbosch, Chris Toebes, Hans van den Vlekkert, et al. A 12-mode universal photonic processor for quantum information processing. *arXiv preprint arXiv:2012.05673*, 2020.
- [32] Mathias Pont, Riccardo Albiero, Sarah E Thomas, Nicolò Spagnolo, Francesco Ceccarelli, Giacomo Corrielli, Alexandre Brioussel, Niccolò Somaschi, Hélio Huet, Abdelmounaim Harouri, et al. Quantifying n-photon indistinguishability with a cyclic integrated interferometer. *Physical Review X*, 12(3):031033, 2022.
- [33] Nicolas Heurtel, Andreas Fyrrillas, Grégoire de Gliniasty, Raphaël Le Bihan, Sébastien Malherbe, Marceau Pailhas, Eric Bertasi, Boris Bourdoncle, Pierre-Emmanuel Emeriau, Rawad Mezher, et al. Perceval: A software platform for discrete variable photonic quantum computing. *Quantum*, 7:931, 2023.
- [34] Roel Burgwal, William R. Clements, Devin H. Smith, James C. Gates, W. Steven Kolthammer, Jelmer J. Renema, and Ian A. Walmsley. Using an imperfect photonic network to implement random unitaries. *Optics Express*, 25(23):28236–28245, Nov 2017. ISSN 1094-4087. doi: 10.1364/OE.25.028236.
- [35] Nicholas J. Russell, Levon Chakhmakhchyan, Jeremy L. O’Brien, and Anthony Laing. Direct dialling of haar random unitary matrices. *New Journal of Physics*, 19(3): 033007, Mar 2017. ISSN 1367-2630. doi:10.1088/1367-2630/aa60ed.
- [36] Emanuel Knill, Raymond Laflamme, and Gerald J Milburn. A scheme for efficient quantum computation with linear optics. *nature*, 409(6816):46–52, 2001.
- [37] Michael A Nielsen and Isaac Chuang. Quantum computation and quantum information, 2002.
- [38] Benoît Collins and Piotr Śniady. Integration with respect to the haar measure on unitary, orthogonal and symplectic group. *Communications in Mathematical Physics*, 264(3):773–795, 2006.
- [39] Easwar Magesan, Jay M Gambetta, and Joseph Emerson. Characterizing quantum gates via randomized benchmarking. *Physical Review A*, 85(4):042311, 2012.
- [40] Christoph Dankert, Richard Cleve, Joseph Emerson, and Etera Livine. Exact and approximate unitary 2-designs and their application to fidelity estimation. *Physical Review A*, 80(1):012304, 2009.
- [41] Alexandre Clément, Nicolas Heurtel, Shane Mansfield, Simon Perdrix, and Benoît Valiron. Lov-calculus: A graphical language for linear optical quantum circuits. *arXiv preprint arXiv:2204.11787*, 2022.
- [42] Rawad Mezher and Stephen Wein. Direct computing of the average gate fidelity of any gate. *Manuscript in preparation*, 2023.
- [43] Masoud Mohseni, Ali T Rezakhani, and Daniel A Lidar. Quantum-process tomography: Resource analysis of different strategies. *Physical Review A*, 77(3):032322, 2008.
- [44] Sergey Bravyi and Alexei Kitaev. Universal quantum computation with ideal clifford gates and noisy ancillas. *Physical Review A*, 71(2):022316, 2005.
- [45] Alberto Peruzzo, Jarrod McClean, Peter Shadbolt, Man-Hong Yung, Xiao-Qi Zhou, Peter J Love, Alán Aspuru-Guzik, and Jeremy L O’Brien. A variational eigenvalue solver on a photonic quantum processor. *Nature communications*, 5(1):4213, 2014.
- [46] Jules Tilly, Hongxiang Chen, Shuxiang Cao, Dario Picozzi, Kanav Setia, Ying Li, Edward Grant, Leonard Wossnig, Ivan Rungger, George H Booth, et al. The variational quantum eigensolver: a review of methods and best practices. *Physics Reports*, 986:1–128, 2022.
- [47] Sergey Bravyi, Jay M Gambetta, Antonio Mezza-capo, and Kristan Temme. Tapering off qubits to simulate fermionic hamiltonians. *arXiv preprint arXiv:1701.08213*, 2017.
- [48] Jarrod R McClean, Nicholas C Rubin, Kevin J Sung, Ian D Kivlichan, Xavier Bonet-Monroig, Yudong Cao, Chengyu Dai, E Schuyler Fried, Craig Gidney, Brendan Gimby, et al. Openfermion: the electronic structure package for quantum computers. *Quantum Science and Technology*, 5(3):034014, 2020.
- [49] Donghwa Lee, Jinil Lee, Seongjin Hong, Hyang-Tag Lim, Young-Wook Cho, Sang-Wook Han, Hyundong Shin, Junaid ur Rehman, and Yong-Su Kim. Error-mitigated photonic variational quantum eigensolver using a single-photon ququart. *Optica*, 9(1):88–95, 2022.
- [50] Jarrod R McClean, Jonathan Romero, Ryan Babbush, and Alán Aspuru-Guzik. The theory of variational hybrid quantum-classical algorithms. *New Journal of Physics*, 18(2):023023, 2016. doi:10.1088/1367-2630/18/2/023023.
- [51] Beng Yee Gan, Daniel Leykam, and Dimitris G. Angelakis. Fock state-enhanced expressivity of quantum machine learning models. *EPJ Quantum Technology*, 9(1), 2022. doi:10.1140/epjqt/s40507-022-00135-0.
- [52] R. A. Fisher. The use of multiple measurements in taxonomic problems. *Annals of Eugenics*, 7(2):179–188, 1936. doi:https://doi.org/10.1111/j.1469-1809.1936.tb02137.x.
- [53] Vojtěch Havlíček, Antonio D. Córcoles, Kristan Temme, Aram W. Harrow, Abhinav Kandala, Jerry M. Chow, and Jay M. Gambetta. Supervised learning with quantum-enhanced feature spaces. *Nature*, 567(7747):209–212, 2019. doi:10.1038/s41586-019-0980-2.
- [54] Karol Bartkiewicz, Clemens Gneiting, Antonín Černoch, Kateřina Jiráková, Karel Lemr, and Franco Nori. Experimental kernel-based quantum machine learning in finite feature space. *Scientific Reports*, 10(1), 2020. doi: 10.1038/s41598-020-68911-5.
- [55] Scott Aaronson and Alex Arkhipov. The computational complexity of linear optics. *Proceedings of the forty-third annual ACM symposium on Theory of computing*, pages 333–342, 2011.
- [56] Craig S Hamilton, Regina Kruse, Linda Sansoni, Sonja Barkhofen, Christine Silberhorn, and Igor Jex. Gaussian boson sampling. *Physical review letters*, 119(17):170501, 2017.
- [57] Han-Sen Zhong, Yuan Li, Wei Li, Li-Chao Peng, Zu-En Su, Yi Hu, Yu-Ming He, Xing Ding, Weijun Zhang, Hao Li, et al. 12-photon entanglement and scalable scatter-shot boson sampling with optimal entangled-photon

- pairs from parametric down-conversion. *Physical review letters*, 121(25):250505, 2018.
- [58] Stefano Paesani, Yunhong Ding, Raffaele Santagati, Levon Chakhmakhchyan, Caterina Vigliar, Karsten Rottwitt, Leif K Oxenløwe, Jianwei Wang, Mark G Thompson, and Anthony Laing. Generation and sampling of quantum states of light in a silicon chip. *Nature Physics*, 15(9):925–929, 2019.
- [59] Jun Gao, Zhi-Qiang Jiao, Ruo-Jing Ren, Xiao-Wei Wang, Xiao-Yun Xu, Wen-Hao Zhou, Lu-Feng Qiao, and Xian-Min Jin. Experimental collision-free dominant boson sampling. *arXiv preprint arXiv:1910.11320*, 2019.
- [60] Francesco Hoch, Simone Piacentini, Taira Giordani, Zhen-Nan Tian, Mariagrazia Iuliano, Chiara Esposito, Anita Camillini, Gonzalo Carvacho, Francesco Ceccarelli, Nicolò Spagnolo, et al. Reconfigurable continuously-coupled 3d photonic circuit for boson sampling experiments. *npj Quantum Information*, 8(1):55, 2022.
- [61] Scott Aaronson and Alex Arkhipov. Bosonsampling is far from uniform. *arXiv preprint arXiv:1309.7460*, 2013.
- [62] Nicolo Spagnolo, Chiara Vitelli, Marco Bentivegna, Daniel J Brod, Andrea Crespi, Fulvio Flamini, Sandro Giacomini, Giorgio Milani, Roberta Ramponi, Paolo Mataloni, et al. Experimental validation of photonic boson sampling. *Nature Photonics*, 8(8):615–620, 2014.
- [63] Hui Wang, Wei Li, Xiao Jiang, Y-M He, Y-H Li, Xing Ding, M-C Chen, Jian Qin, C-Z Peng, Christian Schneider, et al. Toward scalable boson sampling with photon loss. *Physical review letters*, 120(23):230502, 2018.
- [64] Bi-Ying Wang, Emil V Denning, Uğur Meriç Gür, Chao-Yang Lu, and Niels Gregersen. Micropillar single-photon source design for simultaneous near-unity efficiency and indistinguishability. *Physical Review B*, 102(12):125301, 2020.
- [65] Timothy C Ralph, Nathan K Langford, TB Bell, and AG White. Linear optical controlled-not gate in the coincidence basis. *Physical Review A*, 65(6):062324, 2002.
- [66] Clément Gouriou. Design and fabrication of an integrated photonic circuit for producing a maximally-entangled three-photon state. 2019. URL <http://hdl.handle.net/10589/151271>.
- [67] Marc Hein, Wolfgang Dür, Jens Eisert, Robert Raussendorf, M Nest, and H-J Briegel. Entanglement in graph states and its applications. *arXiv preprint quant-ph/0602096*, 2006.
- [68] H Ollivier, SE Thomas, SC Wein, I Maillette de Buy Wenniger, N Coste, JC Loredo, N Somaschi, A Harouri, A Lemaitre, I Sagnes, et al. Hong-oumandel interference with imperfect single photon sources. *Physical Review Letters*, 126(6):063602, 2021.
- [69] O Gazzano, S Michaelis de Vasconcellos, C Arnold, A Nowak, E Galopin, I Sagnes, L Lanco, A Lemaître, and P Senellart. Bright solid-state sources of indistinguishable single photons. *Nature communications*, 4(1):1425, 2013.
- [70] H Snijders, JA Frey, J Norman, VP Post, AC Gosard, JE Bowers, MP Van Exter, W Löffler, and D Bouwmeester. Fiber-coupled cavity-qed source of identical single photons. *Physical Review Applied*, 9(3):031002, 2018.
- [71] Giuseppe Della Valle, Roberto Osellame, and Paolo Laporta. Micromachining of photonic devices by femtosecond laser pulses. *Journal of Optics A: Pure and Applied Optics*, 11(1):013001, 2008.
- [72] C Antón, Juan Carlos Loredo, Guillaume Coppola, Helene Ollivier, Niko Viggianiello, Abdelmounaim Harouri, Niccolo Somaschi, Andrea Crespi, Isabelle Sagnes, Aris-tide Lemaitre, et al. Interfacing scalable photonic platforms: solid-state based multi-photon interference in a reconfigurable glass chip. *Optica*, 6(12):1471–1477, 2019.
- [73] Daniel J Brod, Ernesto F Galvão, Andrea Crespi, Roberto Osellame, Nicolò Spagnolo, and Fabio Sciarrino. Photonic implementation of boson sampling: a review. *Advanced Photonics*, 1(3):034001–034001, 2019.
- [74] Joseph M Renes, Robin Blume-Kohout, Andrew J Scott, and Carlton M Caves. Symmetric informationally complete quantum measurements. *Journal of Mathematical Physics*, 45(6):2171–2180, 2004.
- [75] Aram W Harrow. The church of the symmetric subspace. *arXiv preprint arXiv:1308.6595*, 2013.
- [76] Jeremy L O’Brien, Geoff J Pryde, Alexei Gilchrist, Daniel FV James, Nathan K Langford, Timothy C Ralph, and Andrew G White. Quantum process tomography of a controlled-not gate. *Physical review letters*, 93(8):080502, 2004.
- [77] Michael A Nielsen. A simple formula for the average gate fidelity of a quantum dynamical operation. *Physics Letters A*, 303(4):249–252, 2002.
- [78] Michał Horodecki, Paweł Horodecki, and Ryszard Horodecki. General teleportation channel, singlet fraction, and quasidistillation. *Physical Review A*, 60(3):1888, 1999.
- [79] Steven T Flammia and Yi-Kai Liu. Direct fidelity estimation from few pauli measurements. *Physical review letters*, 106(23):230501, 2011.
- [80] Weikang Li and Dong-Ling Deng. Recent advances for quantum classifiers. *Science China Physics, Mechanics & Astronomy*, 65(2), dec 2021. doi:10.1007/s11433-021-1793-6. URL <https://doi.org/10.1007/s11433-021-1793-6>.
- [81] Michael Reck, Anton Zeilinger, Herbert J. Bernstein, and Philip Bertani. Experimental realization of any discrete unitary operator. *Phys. Rev. Lett.*, 73:58–61, Jul 1994. doi:10.1103/PhysRevLett.73.58. URL <https://link.aps.org/doi/10.1103/PhysRevLett.73.58>.
- [82] William R. Clements, Peter C. Humphreys, Benjamin J. Metcalf, W. Steven Kolthammer, and Ian A. Walmsley. Optimal design for universal multiport interferometers. *Optica*, 3(12):1460–1465, Dec 2016. doi:10.1364/OPTICA.3.001460. URL <https://opg.optica.org/optica/abstract.cfm?URI=optica-3-12-1460>.
- [83] Jacob T Seeley, Martin J Richard, and Peter J Love. The bravyi-kitaev transformation for quantum computation of electronic structure. *The Journal of chemical physics*, 137(22):224109, 2012.
- [84] Peter JJ O’Malley, Ryan Babbush, Ian D Kivlichan, Jonathan Romero, Jarrod R McClean, Rami Barends, Julian Kelly, Pedram Roushan, Andrew Tranter, Nan Ding, et al. Scalable quantum simulation of molecular energies. *Physical Review X*, 6(3):031007, 2016.
- [85] Junaid ur ur Rehman and Hyundong Shin. Entanglement-free parameter estimation of generalized pauli channels. *Quantum*, 5:490, 2021.

METHODS

Architecture

Ascella is accessible remotely via a cloud service [28]. Tasks can be dispatched either to Ascella, to a perfect simulator or to a noisy simulator through a generic scheduler handling user access limitations and task prioritization. Following a compilation and transpilation process, Ascella then sets the demultiplexer configuration and the photonic circuit phases to apply the required unitary matrix to the input state. For applications like quantum machine learning (QML) for which each training data sample corresponds to a task, users can prepare and send a batch of tasks that will execute sequentially on the QPU with fast incremental chip reconfiguration and without any communication overhead.

Chip control benchmarking

We benchmark the transpilation process by applying 300 random phase configurations on the photonic chip and measuring the photon countrates at the 12 outputs. We compare them to a simulation of the chip which is takes into account the estimated directional coupler reflectivities and relative output losses (see Supplementary S-IV for values). We quantify the difference between the measured and simulated values using the total variation distance (TVD). At 925 nm, with a standard characterization of the chip based on interference fringes measurements [31], the TVD evaluated on the configurations is $(21 \pm 11) \%$, where the error bar is the standard deviation of the dataset. At the operating wavelength of our single-photon source (928 nm), with our machine learning process, we achieve a TVD of $(3.0 \pm 1.3) \%$, greatly improving our control over the chip. The relative variation on the obtained average TVD between successive benchmarkings is of the order of 3 %, showing repeatability of the obtained value.

Variational Quantum Eigensolver

The ansatz for the VQE algorithm implements the gate-based circuit shown in Fig. 2.a which consists of a generic 2-qubit state generator. It comprises single-qubit rotations and a CNOT gate [65]. This is implemented on 6 modes (modes 1 to 6) comprising two path-encoded qubits and two extra modes for the postselected Ralph CNOT. Arbitrary rotations are implemented via tunable Mach-Zehnder interferometers with thermo-optic phase shifters. Extra phase shifters are used to mitigate systematic errors in the reflectivity of beamsplitters and to converge faster to the ground state energy.

Boson Sampling

Two statistical tests are used to discriminate the experimental data against the uniform sampler and distinguishable particle hypotheses. The A & A counter and the likelihood ratio counter, respectively, are increased or decreased according to a likelihood ratio test. The A & A counter A is defined as [60, 61]

$$A_k := \begin{cases} A_{k-1} + 1 & \text{if } \mathcal{P} \geq \left(\frac{n}{m}\right)^2 \\ A_{k-1} - 1 & \text{if } \mathcal{P} < \left(\frac{n}{m}\right)^2 \end{cases}$$

where n and m are, respectively, the number of photons and optical modes, and $\mathcal{P} := \prod_i \sum_j |U_{ij}|^2$, where i labels the modes in which photons are detected, j the input modes and U is the unitary sampling matrix.

The likelihood ratio counter C is defined as [60, 62]

$$C_k := \begin{cases} C_{k-1} + 1 & \text{if } \mathcal{L} \geq \left(\frac{n}{m}\right)^2 \\ C_{k-1} - 1 & \text{if } \mathcal{L} < \left(\frac{n}{m}\right)^2 \end{cases}$$

where $\mathcal{L} := \frac{q}{p}$ with $q := |\text{Perm}(U_{(ij)})|^2$, $p := |\text{Perm}(U_{(ij)})|^2$ and $U_{(ij)}$ denoting the sub-matrix restricted to the input labels i and output labels j .

Photon-based quantum neural network

We build the ansatz of our variational quantum classifier using modes 3 to 7 of Ascella. We input three photons into the chip, in modes 3, 5 and 7. We use 32 of the reconfigurable thermo-optic phase shifters as the variational parameters, and 4 phase shifters in the middle of the chip for the data encoding. We use extra modes for pseudo photon-number resolution (PNR): by setting four phase shifters to $\pi/2$ in the final layer of the chip, we redirect a portion of the photons from modes 3 and 7 into modes 1, 2 and 8, 9 respectively. For the classical optimization process, we use a see-saw approach based on Gaussian processes and Nelder-Mead optimizers. More details regarding the circuit ansatz, model definition, pseudo PNR, and the optimization methods are in Supplementary S-VII.

Heralded three-photon GHZ on-chip generation

The generation of a path-encoded 3-photon GHZ state is characterized with three reconfigurable integrated Mach-Zehnder interferometers (MZI_{*i*}, $i = 1, 2, 3$). The layout of the optical circuit is provided in the Supplementary S-IX. The output state of the circuit is given

by [66]

$$|\text{Out}\rangle = \frac{1}{16}(-|\text{GHZ}_3^-\rangle |h_1\rangle + |\text{GHZ}_3^-\rangle [|h_4\rangle + |h_6\rangle + |h_7\rangle] - i|\text{GHZ}_3^+\rangle |h_8\rangle + i|\text{GHZ}_3^+\rangle [|h_2\rangle + |h_3\rangle + |h_5\rangle]).$$

We target the state $|\text{GHZ}_3^+\rangle$, where $|\text{GHZ}_3^\pm\rangle = (|000\rangle \pm |111\rangle)/\sqrt{2}$, which is obtained by conditioning the analysis of the state on the detection of one of the heralding states $|h_2\rangle$, $|h_3\rangle$, $|h_5\rangle$, and $|h_8\rangle$.

The heralding channels signal the generation of a specific GHZ state. The heralding conditions for the generation of $|\text{GHZ}_3^+\rangle$ are

$$\begin{cases} |h_2\rangle = |0_21_30_41_71_80_9\rangle \\ |h_3\rangle = |1_20_30_41_70_81_9\rangle \\ |h_5\rangle = |1_20_31_40_71_80_9\rangle \\ |h_8\rangle = |0_21_31_40_70_81_9\rangle \end{cases}$$

where $|0_i\rangle$ ($|1_i\rangle$) correspond to detecting 0 (1) photons in mode i (modes are labelled from 1 to 12 from top to bottom).

The state $|\text{GHZ}_3^+\rangle$ is a stabiliser state, and therefore can uniquely be expressed in terms of its stabilisers [67].

$$|\text{GHZ}_3^+\rangle \langle \text{GHZ}_3^+| = \sum_{S_i \in \mathcal{S}} \frac{1}{|\mathcal{S}|} S_i, \quad (2)$$

where S_i is a stabiliser of $|\text{GHZ}_3^+\rangle$, \mathcal{S} is the stabiliser group of $|\text{GHZ}_3^+\rangle$, and $|\mathcal{S}|$ is the number of elements of \mathcal{S} . The fidelity of some experimental implementation ρ of $|\text{GHZ}_3^+\rangle$ is given by

$$F_{\text{GHZ}_3^+} = \text{Tr}(|\text{GHZ}_3^+\rangle \langle \text{GHZ}_3^+| \rho),$$

Plugging the expansion of $|\text{GHZ}_3^+\rangle \langle \text{GHZ}_3^+|$ into $F_{\text{GHZ}_3^+}$ and using linearity of the trace, one obtains

$$F_{\text{GHZ}_3^+} = \frac{1}{|\mathcal{S}|} \sum_{S_i \in \mathcal{S}} \text{Trace}(S_i \rho) = \frac{1}{|\mathcal{S}|} \sum_{S_i \in \mathcal{S}} \langle S_i \rangle.$$

Supplementary Information

S-I. SINGLE-PHOTON SOURCE

The single-photon source is based on a gated InGaAs quantum dot (QD) embedded in a monolithic micropillar cavity [20] cooled down to 5K. It is optically excited using the near-resonant LA-phonon-assisted excitation scheme [29] at an 80 MHz rate. The neutral QD emits linearly-polarized single photons at 928 nm with a lifetime of 92 ps and a 55% first lens brightness. After spectrally filtering the remaining excitation laser using free-space spectral bandpass filters (FWHM=800 pm) and coupling into a single mode fiber, the single-photon source device shows a low multiphoton component with a single-photon purity $\mathcal{P} = 1 - g^{(2)}(0) > 99\%$ and a 2-photon indistinguishability $M_s > 94\%$.

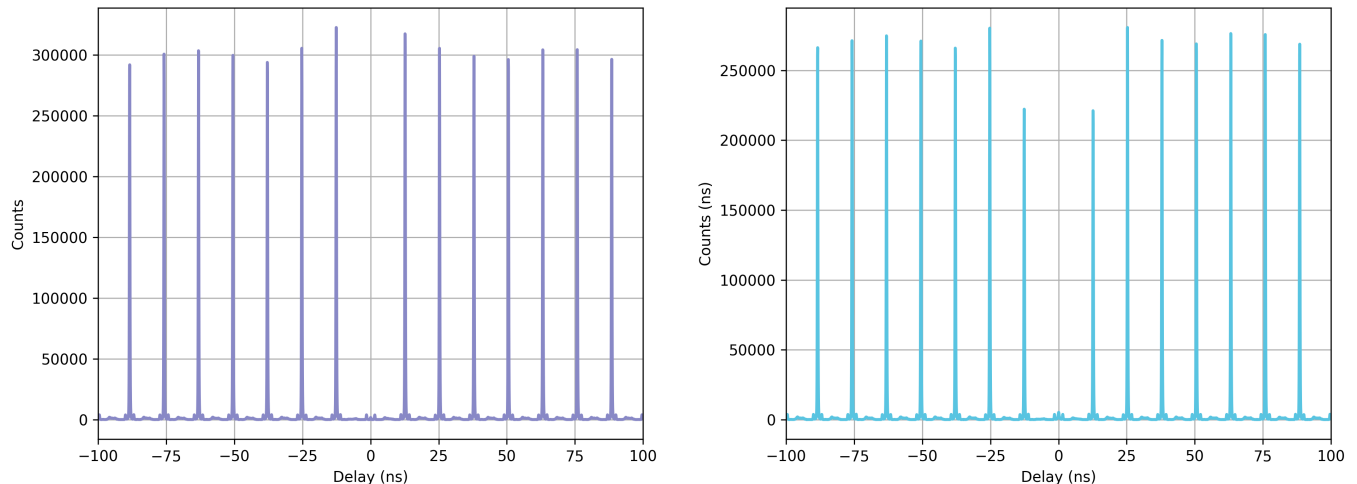


FIG. S1: **The single-photon source delivers pure and indistinguishable single photons.** Single-photon purity is quantified by the normalized second-order correlation function $g^{(2)}(0) = (7.32 \pm 0.07) \times 10^{-3}$ (left) and the Hong-Ou-Mandel visibility $V_{\text{HOM}} = 0.9296 \pm 0.0003$ (right) yielding a corrected 2-photon indistinguishability of $M_s = 0.9438 \pm 0.0003$ [68]. The histograms were integrated for 5 s and the peak integration window is 1 ns. The integrated values are obtained with no background subtraction.

S-II. OPTICAL SETUP

The overall transmission of the optical setup (see Fig. 1.a) is characterized by the transmission or efficiency of each module. A precise loss budget of the optical setup is provided in Tab. S1.

Module	Transmission/Efficiency	Near-term targets
First lens brightness	55 %	80% [69]
Single-mode fiber coupling	70 %	85% [70]
Spectral Filtering module	75 %	>82%[*]
Demultiplexer	70 %	>80%[*]
PIC insertion and transmission	45 %	70% [71]
SNSPDs	92 %	>95%**]
Total	8.4 ± 0.2 %	27%
Pump laser repetition rate	80 MHz	320 MHz [72]
6-photon countrate	4 Hz	~35 kHz (computed)
12-photon countrate	200 nHz (computed)	~10 Hz (computed)

TABLE S1: Current loss budget of the optical setup (Transmission/Efficiency) and near-term targets. [*] Optical module in development at Quandela. [**] Commercially available products

Because the photon input ports on the chip are maintained fixed, the transpilation process also uses the chip's universality to input arbitrary photon configurations by implementing in reality unitary matrices of the type $\hat{U} \times \hat{U}_{\text{perm}}$, where \hat{U} is the initial unitary matrix and \hat{U}_{perm} a permutation matrix yielding the required photon input configuration. If less than 6 photons are needed, mechanical shutters block the paths of additional photons at the demultiplexing stage.

Ascella's detection module is composed of superconducting nanowire single-photon detectors showing an average detection efficiency of 92 % and dark countrates under 20 Hz. Detection events are digitalized using a time-to-digital converter (Swabian instruments) and post-processed for sampling N -photon ($1 \leq N \leq 6$) coincidences between all 12 detectors within a 1 ns coincidence window.

The polarization in the delay fibers is optimized automatically to ensure a maximal transmission to the polarization-selective photonic circuit. The excitation laser power is similarly stabilized, ensuring optimal brightness and photon purity.

S-III. MULTIPHOTON INTERFERENCE CHARACTERIZATION

In this section, we measure all pairwise 2-photon indistinguishabilities, and the *genuine* 4- and 6-photon indistinguishability of the input state of Ascella, i.e. the probability that the n ($n = 4$ or $n = 6$) photons are identical [32, 73]. This initial characterization of our input state sets the basis for future practical applications on our platform. It also allows us to fine-tune our simulator to be able to reproduce experimental results with a good agreement.

We first measure the 2-photon pairwise indistinguishability M_{ij} ($i, j = 1, \dots, 6$) between all $C_6^2 = 15$ photon pairs. The reconfigurable chip is set to successively connect each pair with a Mach-Zehnder interferometer (MZI). We vary the internal phase of the MZI to measure the correlated $\phi = \pi/2$ (uncorrelated $\phi = \pi$) 2-photon coincidences at zero time delay, which gives access to the visibility of the 2-photon interference fringe. The imperfect single-photon purity [68] of our QD-source ($g^{(2)}(0) = 0.0075$), is taken into account to compute M_{ij} for all 15 pairs. The values of M_{ij} for each of the 15 pairs is reported in the *indistinguishability matrix* \mathcal{M} where $\mathcal{M}_{ij} = M_{ij}$ and $\mathcal{M}_{ii} = 1$.

$$\mathcal{M} = \begin{bmatrix} 1 & 0.942 & 0.921 & 0.924 & 0.917 & 0.914 \\ & \ddots & 0.935 & 0.925 & 0.924 & 0.919 \\ & & \ddots & 0.932 & 0.911 & 0.925 \\ & & & \ddots & 0.943 & 0.941 \\ & & & & \ddots & 0.942 \\ & & & & & 1 \end{bmatrix}$$

The genuine N -photon indistinguishability is the probability p_N that all N photons are identical. To quantify experimentally the genuine 4- and 6-photon indistinguishability of our input multiphoton state we implement on the reconfigurable QPU 8-mode and 12-mode versions of the cyclic interferometer (first introduced in [32]) whose general layout is presented in Fig. S2.a. First, the single internal phase of the interferometer α is set to 0 (2π). Each odd input port of the interferometer is fed with single photons. We detect the output states corresponding to one photon per pair of output ports ($2k, 2k + 1$) (see Fig. S2.a). In Fig. S2.b-c we present the experimental output distribution for all outputs corresponding to constructive (orange) and destructive (blue) n -photon interference ($N = 4$ for b. and $N = 6$ for c.). The visibility of the interference fringe is the genuine N -photon indistinguishability. We experimentally measure $p_4 = 0.85 \pm 0.002$ 4-photon indistinguishability for photons $\{1, 2, 3, 4\}$ and $p_6 = 0.76 \pm 0.02$ 6-photon indistinguishability. This work constitutes the first experimental realization of this protocol for 6 photons, and sets a new state-of-the-art for genuine 4- and 6-photon indistinguishability.

To further study our ability to drive the internal phase of the interferometer shown in Fig. S2.a, we scan the single internal phase α to measure the full interference fringe visibility for 4-photon interferences with photons $\{1, 2, 3, 4\}$. Note that for each value of the internal phase α we compute the associated unitary matrix using *Perceval* and transpile the circuit to be implemented on the QPU. After normalization of the 4-photon counts, we fit the theoretical interference fringe [32] $p_4 = 1 \pm c_1 \cos(a \cdot \alpha + b)$. In the ideal case we expect $a_{\text{ideal}} = 1$ and $b_{\text{ideal}} = 0$. The experimental data is well fitted with $a = 1.00 \pm 0.01$ and $b = -0.06 \pm 0.08$ rad, which shows that the transpilation can very accurately implement an 8×8 unitary matrix.

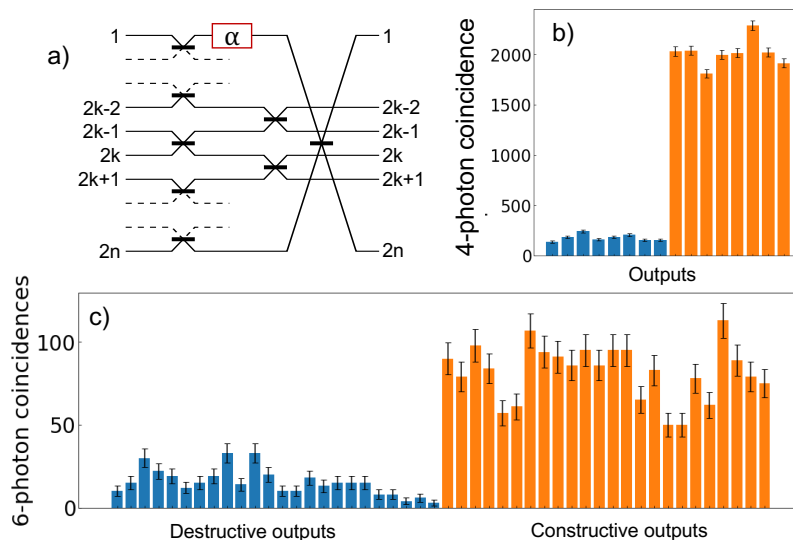


FIG. S2: Genuine indistinguishability of the input multiphoton state. (a) General layout of the multiport interferometer used to measure the probability that the N photons are identical. (b-c) Histogram of 4- (6-) photon outputs that undergo destructive (blue) and constructive (orange) interferences in an 8- (12-) mode version of the interferometer presented in (a) fed with 4 (6) photons. In (b) the genuine 4-photon indistinguishability is $p_4 = 0.85 \pm 0.02$. In (c) the genuine 6-photon indistinguishability is $p_6 = 0.76 \pm 0.02$.

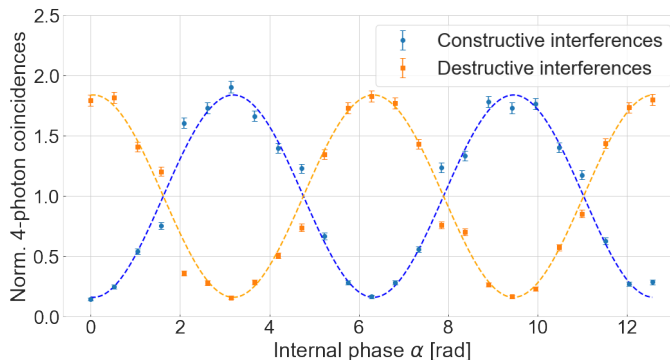


FIG. S3: Total normalized four-photon coincidence rate (sum of all eight output states) for the constructive and destructive outputs, as a function of the internal phase α . The error bars are computed assuming a shot noise limited error on the detected 4-fold coincidences

S-IV. PHOTONIC CHIP CHARACTERIZATION

We use a machine learning-based process to characterize the photonic chip. The 126 on-chip thermo-optic phase shifters generate heat via the Joule effect, thus they can be modelled by a relation of the form $\vec{\phi} = A\vec{V}^{\odot 2} + \vec{b}$ between the vector $\vec{\phi}$ containing all 126 physically implemented phases and the vector \vec{V} corresponding to the 126 applied voltages squared. \odot^2 represents element-wise squaring. Off-diagonal elements of the 126×126 matrix A represent thermal crosstalk between phase shifters. A process based on machine-learning techniques optimizes the values of A and \vec{b} , which represent ≈ 16000 free parameters to determine. The same process also estimates individual directional coupler reflectivities and relative output losses. We show on Fig. S8 the estimated values. The elements of \vec{b} have values (0.1 ± 1.2) rad, and the diagonal elements of A have values (0.034 ± 0.001) rad/V², ensuring that on average a π -phase shift can be achieved by applying around 10 V on a phase shifter. The matrix A seems to show long-range interactions between phase shifters, but these are, in reality, artefacts arising from certain transformations on A that leave the output quantum state unchanged. The directional coupler reflectivities have values $(56.8 \pm 0.6)\%$. One can observe regions of low and high reflectivities on Fig. S6, which is a signature of the photonic chip's folding; that is the interferometer is not laid out in a straight manner, but is folded to increase compactness. For the output losses,

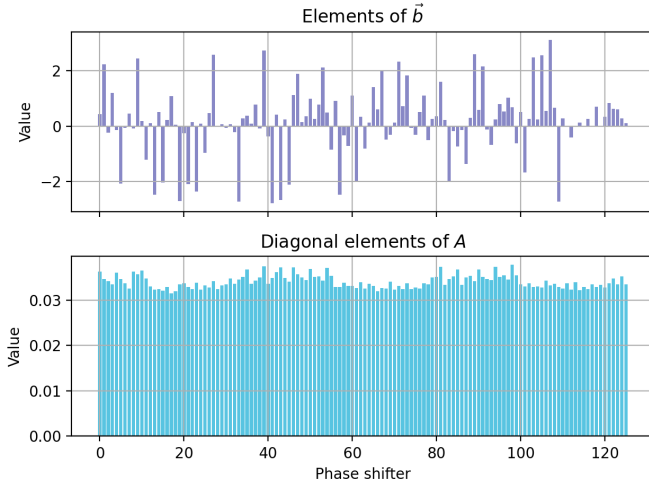


FIG. S4

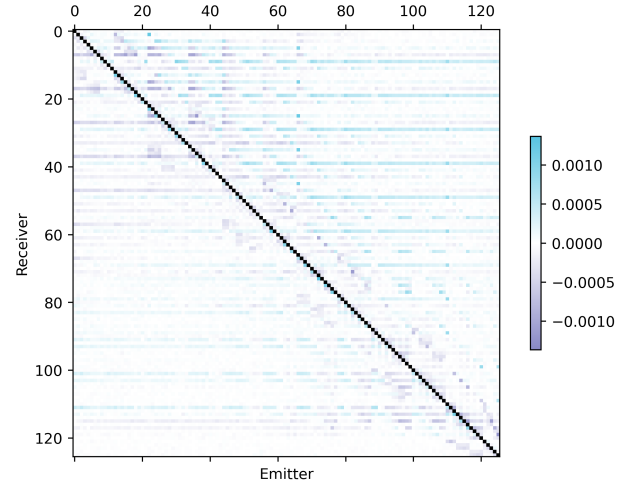


FIG. S5

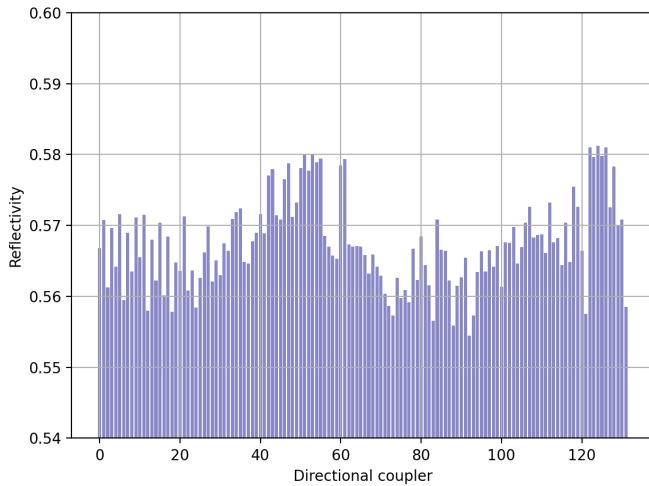


FIG. S6

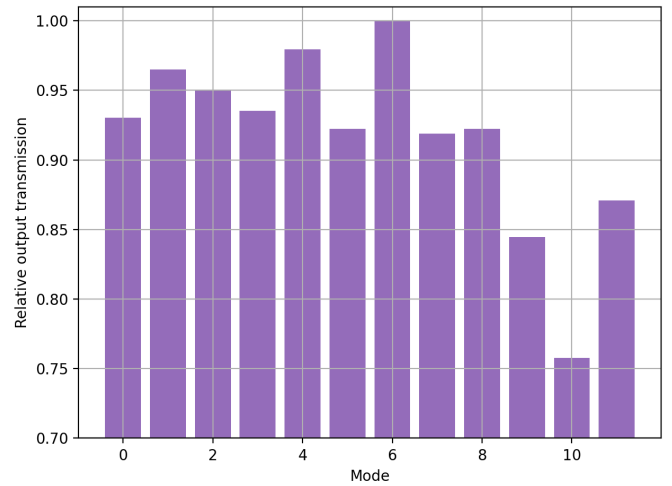


FIG. S7

FIG. S8: Large-scale photonic chip imperfections estimated by a machine-learning process. The phase shifter phase-voltage relation is modelled by a matrix relation of the form $\vec{\phi} = A\vec{V}^{\odot 2} + \vec{b}$, where $\vec{\phi}$ and $\vec{V}^{\odot 2}$ are vectors containing respectively the applied phase shifts and squared voltages. We show on S4 the diagonal elements of A and the elements of \vec{b} , and on S5 we show the off-diagonal elements of A , which account for thermal crosstalk. S6 represents the values of the reflectivity of the on-chip directional couplers. S7 displays the relative output losses per mode, scaled such that the maximum value is equal to 1.

we notice that mode 10 has a relative transmission of 75% compared to mode 6. This result was confirmed on two separate detection systems (power meter array and single-photon detectors), hinting that the defect lies in the photonic chip and not in the photon detectors.

S-V. BENCHMARKING LOGIC GATES

In this supplementary section, we outline the method of Ref. [42] applied to benchmark 1-, 2-, and 3- qubit gates implemented by Ascella. We then give an explicit example of the method by deriving F_{avg} for the T -gate. Finally, we describe the general approach taken to obtain F_{avg} for multi-qubit gates and discuss the application to the 2- and 3-qubit gates benchmarked in the main text.

Symmetry-based benchmarking

Let $|\mathbf{i}\rangle := |i_1, \dots, i_n\rangle$ with $i_j \in \{0, 1\}$ for $j \in \{1, \dots, n\}$ denote an n -qubit computational basis state. A noisy implementation of the gate unitary U is given by $\Lambda \circ \mathbf{U}(\cdot)$, which is a completely positive trace preserving (CPTP) map [37] acting on n -qubit density matrices ρ as $\Lambda \circ \mathbf{U}(\rho) = \Lambda(U\rho U^\dagger)$ where Λ is the noise channel. The average fidelity F_{avg} , over all possible n -qubit states, given Λ corresponding to the noisy application of U is shown in [42] to be

$$F_{\text{avg}}(U) = \frac{1}{2^n(2^n + 1)} \sum_{\mathbf{i}, \mathbf{j}, \mathbf{i}', \mathbf{j}'} (\alpha_{|\mathbf{i}'\rangle\langle \mathbf{j}'|; |\mathbf{i}\rangle\langle \mathbf{j}|}^{U^\dagger} + \alpha_{|\mathbf{i}'\rangle\langle \mathbf{j}'|; |\mathbf{j}\rangle\langle \mathbf{i}|}^{U^\dagger}) \text{Trace}[|\mathbf{i}\rangle\langle \mathbf{j}| \Lambda \circ \mathbf{U}(|\mathbf{i}'\rangle\langle \mathbf{j}'|)], \quad (\text{S1})$$

where

the coefficients $\alpha_{|\mathbf{i}'\rangle\langle \mathbf{j}'|; |\mathbf{i}\rangle\langle \mathbf{j}|}^{U^\dagger} := \langle \mathbf{i}' | U^\dagger | \mathbf{i} \rangle \langle \mathbf{j} | U | \mathbf{j}' \rangle \in \mathbb{C}$ depend only on the unitary U . This expression generally includes 2^{4n} terms, corresponding to 2^{4n} measurements. In the worst case, evaluating $F_{\text{avg}}(U)$ as above requires as many measurements as a full process tomography. However, for most gates of interest, a significant number of α coefficients will vanish, hence requiring many fewer measurements to evaluate the sum in Eq. (S1). A more formal proof of Eq. (S1) will appear in [42], but we will now outline the key technical steps needed to arrive at Eq. (S1).

We start by expanding $U|\psi\rangle = \sum_{\mathbf{i}} \beta_{\mathbf{i}} |\mathbf{i}\rangle$ in the basis $\{|\mathbf{i}\rangle\}$ for any initial state $|\psi\rangle$, with $\beta_{\mathbf{i}} \in \mathbb{C}$. Then, by plugging this into the expression of the final state fidelity $F_\psi(U)$ given in the main text, we obtain

$$F_\psi(U) = \sum_{\mathbf{i}, \mathbf{i}', \mathbf{j}, \mathbf{j}'} \beta_{\mathbf{i}}^* \beta_{\mathbf{i}'}^* \beta_{\mathbf{j}} \beta_{\mathbf{j}'} \langle \mathbf{i} | \Lambda(|\mathbf{j}'\rangle\langle \mathbf{i}'|) | \mathbf{j} \rangle,$$

and therefore

$$F_{\text{avg}}(U) = \sum_{\mathbf{i}, \mathbf{i}', \mathbf{j}, \mathbf{j}'} \mathbb{E}(\beta_{\mathbf{i}}^* \beta_{\mathbf{i}'}^* \beta_{\mathbf{j}} \beta_{\mathbf{j}'} \langle \mathbf{i} | \Lambda(|\mathbf{j}'\rangle\langle \mathbf{i}'|) | \mathbf{j} \rangle),$$

where the expectation values of the product of β coefficients is

$$\mathbb{E}(\beta_{\mathbf{i}}^* \beta_{\mathbf{i}'}^* \beta_{\mathbf{j}} \beta_{\mathbf{j}'} \langle \mathbf{i} | \Lambda(|\mathbf{j}'\rangle\langle \mathbf{i}'|) | \mathbf{j} \rangle) := \int d\psi \beta_{\mathbf{i}}^* \beta_{\mathbf{i}'}^* \beta_{\mathbf{j}} \beta_{\mathbf{j}'} \langle \mathbf{i} | \Lambda(|\mathbf{j}'\rangle\langle \mathbf{i}'|) | \mathbf{j} \rangle (\psi).$$

The quantities $\mathbb{E}(\beta_{\mathbf{i}}^* \beta_{\mathbf{i}'}^* \beta_{\mathbf{j}} \beta_{\mathbf{j}'} \langle \mathbf{i} | \Lambda(|\mathbf{j}'\rangle\langle \mathbf{i}'|) | \mathbf{j} \rangle)$ are the same as those in the expansion in the operator basis $\{|\mathbf{j}\rangle\langle \mathbf{j}'| \langle \mathbf{i}'| \langle \mathbf{i}| \}$ of

$$\Pi := \int d\psi (|\psi\rangle\langle \psi|)^{\otimes 2}.$$

In addition, Π is proportional to the projector onto the symmetric subspace of $(\mathbb{C}^d)^{\otimes 2}$ with $d = 2^n$ [74], and this projector has a known expansion in the basis $\{|\mathbf{j}\rangle\langle \mathbf{j}'| \langle \mathbf{i}'| \langle \mathbf{i}| \}$ [75]. These key insights allow us to compute the coefficients $\mathbb{E}(\beta_{\mathbf{i}}^* \beta_{\mathbf{i}'}^* \beta_{\mathbf{j}} \beta_{\mathbf{j}'} \langle \mathbf{i} | \Lambda(|\mathbf{j}'\rangle\langle \mathbf{i}'|) | \mathbf{j} \rangle)$, to obtain

$$F_{\text{avg}}(U) = \frac{1}{2^n(2^n + 1)} \sum_{\mathbf{i}, \mathbf{j}} (\langle \mathbf{i} | \Lambda(|\mathbf{j}\rangle\langle \mathbf{i}|) | \mathbf{j} \rangle + \langle \mathbf{i} | \Lambda(|\mathbf{i}\rangle\langle \mathbf{j}|) | \mathbf{j} \rangle).$$

The last steps needed to arrive at Eq. (S1) are to note that $\langle \mathbf{i} | \Lambda(|\mathbf{j}\rangle\langle \mathbf{i}|) | \mathbf{j} \rangle = \text{Trace}(|\mathbf{j}\rangle\langle \mathbf{i}| \Lambda(|\mathbf{j}\rangle\langle \mathbf{i}|))$, and then to rewrite $\Lambda = \Lambda \circ \mathbf{U} \circ \mathbf{U}^\dagger$, and finally expand $\mathbf{U}^\dagger(|\mathbf{j}\rangle\langle \mathbf{i}|)$ in the basis $\{|\mathbf{i}'\rangle\langle \mathbf{j}'|\}$ to identify the α coefficients of Eq. (S1).

Following this method, we can derive exact expressions of F_{avg} for any gate unitary as a discrete sum of a finite number of terms. As outlined in the following sections, the exact form of F_{avg} and the number of non-zero terms will depend on U , and these terms can be evaluated using a set of state preparation and measurement settings.

We note that there is in the literature another technique to evaluate F_{avg} using fewer measurements than full process tomography. The approach experimentally implemented in [76] obtains F_{avg} by first measuring an intermediate quantity called the entanglement fidelity [77–79]. In contrast, the symmetry-based method outlined here and used in the main text bypasses computing this intermediate quantity and directly evaluates F_{avg} as a weighted summation of measurements. As discussed below, we notably find that the symmetry-based benchmarking approach requires half as many measurements to benchmark a CNOT gate as were required in [76].

Average fidelity of a T -gate

As an illustration of the method in action, we explicitly compute $F_{\text{avg}}(U)$ for the case of the T -gate, which is a very important gate in the context of magic state distillation protocols for fault-tolerant quantum computing [44]. This gate is defined by the unitary transformation

$$T = \begin{pmatrix} 1 & 0 \\ 0 & e^{i\frac{\pi}{4}} \end{pmatrix}. \quad (\text{S2})$$

In this case, the following relations can directly be verified by taking $n = 1$ and replacing U by T to compute the α coefficients:

$$\begin{aligned} \alpha_{|0\rangle\langle 0|;|0\rangle\langle 0|}^{T^\dagger} &= \alpha_{|1\rangle\langle 1|;|1\rangle\langle 1|}^{T^\dagger} = 1, \\ \alpha_{|0\rangle\langle 1|;|0\rangle\langle 1|}^{T^\dagger} &= e^{i\frac{\pi}{4}}, \quad \alpha_{|1\rangle\langle 0|;|1\rangle\langle 0|}^{T^\dagger} = e^{-i\frac{\pi}{4}}, \\ \alpha_{|i\rangle\langle j|;|i'\rangle\langle j'|}^{T^\dagger} &= 0 \text{ when } i \neq i' \text{ or } j \neq j'. \end{aligned} \quad (\text{S3})$$

Plugging these values into Eq. (S1) for $n = 1$ gives

$$\begin{aligned} F_{\text{avg}}(U) &= \frac{1}{3} \text{Trace} [|0\rangle\langle 0| \Lambda \circ \mathbf{T}(|0\rangle\langle 0|)] + \frac{1}{3} \text{Trace} [|1\rangle\langle 1| \Lambda \circ \mathbf{T}(|1\rangle\langle 1|)] \\ &+ \frac{e^{i\frac{\pi}{4}}}{6} (\text{Trace} [|0\rangle\langle 1| \Lambda \circ \mathbf{T}(|0\rangle\langle 1|)] + \text{Trace} [|0\rangle\langle 1| \Lambda \circ \mathbf{T}(|1\rangle\langle 0|)]) \\ &+ \frac{e^{-i\frac{\pi}{4}}}{6} (\text{Trace} [|1\rangle\langle 0| \Lambda \circ \mathbf{T}(|0\rangle\langle 1|)] + \text{Trace} [|1\rangle\langle 0| \Lambda \circ \mathbf{T}(|1\rangle\langle 0|)]). \end{aligned} \quad (\text{S4})$$

Then, we can note that

$$\begin{aligned} |0\rangle\langle 1| &= |+\rangle\langle +| + i|+_i\rangle\langle +_i| - \frac{1+i}{2}I \\ |1\rangle\langle 0| &= |+\rangle\langle +| - i|+_i\rangle\langle +_i| - \frac{1-i}{2}I, \end{aligned} \quad (\text{S5})$$

where $|+\rangle = (|0\rangle + |1\rangle)/\sqrt{2}$, $|+_i\rangle = (|0\rangle + i|1\rangle)/\sqrt{2}$, and $I = |0\rangle\langle 0| + |1\rangle\langle 1|$. In addition, since $\Lambda \circ \mathbf{T}$ is a CPTP map, then $\Lambda \circ \mathbf{T}(I) = I$, and consequently $\text{Trace} [|1\rangle\langle 0| \Lambda \circ \mathbf{T}(I)] = \text{Trace} [|0\rangle\langle 1| \Lambda \circ \mathbf{T}(I)] = 0$. Thus, we can write the average fidelity in terms of four combinations of state preparations $\mathcal{I} = \{|0\rangle, |1\rangle, |+\rangle, |+_i\rangle\}$ and measurements $\mathcal{M} = \{|0\rangle\langle 0|, |1\rangle\langle 1|, |+\rangle\langle +|, |+_i\rangle\langle +_i|\}$ that can be implemented on Ascella:

$$\begin{aligned} F_{\text{avg}}(U) &= \frac{1}{3} \text{Trace} [|0\rangle\langle 0| \Lambda \circ \mathbf{T}(|0\rangle\langle 0|)] + \frac{1}{3} \text{Trace} [|1\rangle\langle 1| \Lambda \circ \mathbf{T}(|1\rangle\langle 1|)] \\ &- \frac{2}{3\sqrt{2}} \text{Trace} [|+\rangle\langle +| \Lambda \circ \mathbf{T}(|+_i\rangle\langle +_i|)] \\ &+ \frac{2}{3\sqrt{2}} \text{Trace} [|+_i\rangle\langle +_i| \Lambda \circ \mathbf{T}(|+\rangle\langle +|)]. \end{aligned} \quad (\text{S6})$$

Multi-qubit gates

To evaluate Eq. (S1) for any given gate unitary U , we must generalize the approach applied above. This can be done by first pre-computing $\Lambda \circ \mathbf{U}$ in terms of single-qubit Pauli operators $S_j \in \{I, X, Y, Z\}$, and then explicitly evaluating $F_{\text{avg}}(U)$ to significantly reduce the required set of measurements that will ultimately be performed by Ascella. This approach provides a solution for $F_{\text{avg}}(U)$, but it is not necessarily the optimal way to determine the required measurement settings.

To evaluate the process map in terms of measurements that can be performed by Ascella, we can choose to prepare each qubit j independently following $|\psi_j\rangle \in \mathcal{I}$ as for the T -gate and measure each qubit independently following $S_j \in \{I, X, Y, Z\}$. This choice of state preparations and measurements also may not be optimal to minimize the number of measurements for any given gate, but it guarantees a system of 2^{4n} linearly independent equations describing an n -qubit noisy gate:

$$\langle S \rangle_{\Psi} = \text{Trace} [S \Lambda \circ \mathbf{U}(|\Psi\rangle\langle \Psi|)], \quad (\text{S7})$$

where $S = S_1 \otimes S_2 \cdots S_n$ and $|\Psi\rangle = |\psi_1\rangle \otimes |\psi_2\rangle \cdots |\psi_n\rangle$.

For $n \leq 3$, this system can be solved directly using symbolic packages or software such as *Mathematica*. Solving 4-qubit gates or larger would require more advanced numerical methods or analytic simplification to circumvent memory limitations. Hence, although the approach to obtain $F_{\text{avg}}(U)$ is general for any gate and results in equal or fewer required measurements compared to a full process tomography, pre-computing these required measurements is still a hard problem.

Evaluating Eq. (S7) for the CNOT and Toffoli gates provides all elements of the error process Λ in terms of Pauli correlations. By evaluating $F_{\text{avg}}(U)$ using the methods of [42], we obtain a set of 58 (593) correlations for the CNOT (Toffoli) gate. The set of correlations m_i and their weight w_i required for the evaluation of $F_{\text{avg}}(U)$ for a CNOT gate are given in Table S3. These solutions represent a significant reduction over the number of correlations that would be necessary to perform full arbitrary process tomography, which is $2^{4n} = 256$ (4096) for the CNOT (Toffoli) gate.

Since some of the correlations are measured among fewer than n qubits, it is possible to further reduce the number of measurement settings by tracing out some qubits from the measurements obtained from higher-order correlations. For example, $\langle IX \rangle$ can be evaluated from the same data used to compute $\langle ZX \rangle$ by tracing out the first qubit. In this case, assuming all I measurements can be evaluated by recycling the Z measurement data, the number of measurements is reduced to 36 (340) for the CNOT (Toffoli), corresponding to 86% (92%) fewer measurements than for a full process tomography. Recycling the X measurement further reduces this to 34 settings for the CNOT gate. Notably, 34 measurement settings are fewer than half of the 71 settings previously used to benchmark a linear-optical CNOT gate in [76].

Benchmarking results

We applied the symmetry-based benchmarking method to gates implemented by Ascella and also gates implemented on other online quantum computing platforms.

Ascella

For each individual state preparation and measurement (SPAM) configuration, the transpilation process converges to a high-fidelity implementation of the desired unitary. However, one of the assumptions needed to apply symmetry-based benchmarking is that the gate unitary remains unchanged for each SPAM configuration. As a result, re-transpiling the unitary for each setting can introduce a small systematic, but random, error in the estimate of the average gate fidelity.

When benchmarking the T -gate naively, we find that the re-transpilation error can occasionally cause the measured average gate fidelity to exceed 1 by up to 0.1%, implying that the re-transpilation error is on the same order of magnitude as the T -gate error for Ascella. To remove this systematic error, we fix the voltages applied to the specific part of the chip implementing the T -gate so that transpilation process only optimizes the SPAM procedure. As a result, the measured average gate fidelity given in the main text is less than 1 to within the measurement precision, but it also no longer fully benefits from the advantage of the machine-learned transpilation process.

We also observe that implementing multiple T -gates in a row, up to 4 T -gates each implemented by a separate part of the chip, does not significantly decrease the measured average single-qubit gate fidelity. This suggests that the dominant contribution to the remaining T -gate error of 0.4% is likely SPAM error.

Since the systematic error caused by re-transpilation is much smaller than the CNOT and the Toffoli gate errors and on the same order of magnitude as the measurement precision we apply the transpilation process to the entire chip for those cases. It is worth noting that implementing the Toffoli gate already saturates all 12 modes of the chip, meaning that it is not possible to implement SPAM without re-transpiling the part of the chip implementing the Toffoli gate.

Other online platforms

To place Ascella in context, we also apply the same symmetry-based benchmarking for gates implemented by several other online quantum computing platforms (see Table S2). We show in Figure S9 an example of a circuit for running benchmarking on these platforms compared to the equivalent circuit on Ascella.

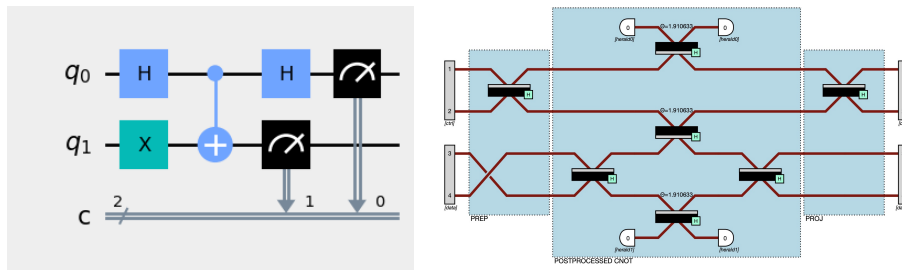


FIG. S9: One of the 36 circuits (+1:XZ), quantum circuit and linear optics circuit equivalent contributing to the 2-qubit CNOT fidelity measurement

Platform (Device)	Gate	F_{avg} (%)	Date - Benchmark Details
Quandela (Ascella)	T-gate	99.6 ± 0.1	2023/05/31 - average and standard deviation on $5 \times 1\text{M}$ -sample measurements, for 14 different gate locations on chip
	CNOT	93.8 ± 0.6	2023/03/20-2023/05/07 - average and standard deviation of 114 consecutive 100k-sample measurements over 46 days
	Toffoli	86 ± 1.2	2023/01/06 - calculated on 100000-sample tasks
IonQ (AWS ionq.qpu)	T-gate	99.6 ± 1	2022/12/16 - calculated on 4096-sample tasks
	CNOT	91.7 ± 1.5	2022/12/17 - calculated on 4096-sample tasks
	Toffoli	90 ± 3.1	2023/01/18 - calculated on 256-sample tasks
Rigetti (AWS rigetti.aspen-11)	T-gate	88.7 ± 1	2022/12/16 - calculated on 4096-sample tasks
	CNOT	71.2 ± 1.5	2022/12/17 - calculated on 4096-sample tasks
IBM (Quito or Belem depending on availability)	T-gate	96 ± 1.5	2022/12/16 - calculated on 4096-sample tasks
	CNOT	86.4 ± 1.5	2022/12/17 - calculated on 4096-sample tasks

TABLE S2: Average gate fidelity F_{avg} obtained from symmetry-based benchmarking applied to devices on other online quantum computing platforms. Margin of uncertainty is based on standard deviation assuming Poisson counting statistics unless otherwise stated. Note that this benchmarking procedure is not robust to SPAM errors, which may be a significant factor for some devices. In addition, the values returned by other online platforms may be post-processed using error mitigation techniques or subject to systematic errors analogous to the re-transpilation errors on Ascella.

S-VI. BOSON SAMPLING

In this section we study boson-sampling with photon loss. With a 6-photon input state, we acquire respectively $295 \cdot 10^9$, $41.5 \cdot 10^9$, $3.07 \cdot 10^9$, $110 \cdot 10^6$, and $1.78 \cdot 10^6$ samples for 1-, 2-, 3-, 4-, and 5-photon coincidences. We compute the total variation distance $D = \frac{1}{2} \sum_i |p_i - q_i|$ where $\{p_i\}$ and $\{q_i\}$ are the ideal and experimental output probability distributions respectively for output states with 2, 3, 4 and 5 photons. The results are reported in Tab. S4. For > 2 photon loss the experimental output probability is dominated by loss, and no longer describe the ideal distribution.

To validate that our boson-sampler device is functioning correctly, we use a phenomenological approach that models all sources of noise in the experimental apparatus and demonstrate that we reach a remarkable overlap between all threshold statistics and our simulations. Using *Perceval*, we develop a realistic simulator for our boson-sampler. We use the phenomenological model first introduced in [30] of our single-photon source to account for the partial distinguishability of the multiphoton state, the imperfect single-photon purity and the optical losses. Then, we account for the error related to the transpilation of the unitary matrix and the imperfect implementation of the physical phases with the thermo-optic phase shifters. The simulations gives a total variation distance of $D_{\text{simu}} = 0.132$ and a fidelity of $F_{\text{simu}} = 0.978$. The simulations are compatible with the experimental data, which shows that our realistic simulator

w_i	m_i	w_i	m_i	w_i	m_i	w_i	m_i	w_i	m_i	w_i	m_i
1	00:II	1	01:II	2	0+:IX	-1	10:YY	1	11:YY	2	+0:YY
-1	00:IX	-1	01:IX	2	0+:XI	-1	10:ZI	-1	11:ZI	2	+1:XI
1	00:IZ	-1	01:IZ	2	0+:ZX	1	10:ZX	1	11:ZX	-2	+1:XX
-1	00:XI	-1	01:XI	-2	0i:XZ	1	10:ZZ	-1	11:ZZ	-2	+1:YY
1	00:XX	1	01:XX	1	10:II	1	11:II	2	1+:IX	-4	++:XI
1	00:XZ	1	01:XZ	-1	10:IX	-1	11:IX	2	1+:XI	-2	i0:XZ
-1	00:YY	1	01:YY	-1	10:IZ	1	11:IZ	-2	1+:ZX	-2	i1:XZ
1	00:ZI	1	01:ZI	-1	10:XI	-1	11:XI	-2	1i:XZ	4	ii:XZ
-1	00:ZX	-1	01:ZX	1	10:XX	1	11:XX	2	+0:XI		
1	00:ZZ	-1	01:ZZ	1	10:XZ	1	11:XZ	-2	+0:XX		

TABLE S3: List of 58 weights w_i and correlations m_i used to evaluate the average fidelity $F_{\text{avg}}(U) = (1/40) \sum_i w_i m_i$ of a CNOT gate. Correlations are labelled by $ab:xy$ where $a, b \in \{0, 1, +, i\}$ represent state preparation ($\{|0\rangle, |1\rangle, |+\rangle, |i\rangle\}$ respectively), and $x, y \in \{I, X, Y, Z\}$ represent measurements ($\{I, X, Y, Z\}$ respectively).

N -photon loss	Fidelity	Distance
0-	0.97±0.03	0.16±0.02
1-	0.989±0.002	0.118
2-	0.9950±0.0002	0.143
3-	0.99625±3e-05	0.225
4-	0.997333±6e-06	0.40

TABLE S4: Fidelity and total variation distance between the experimental data and the ideal output probability for all N -photon outcomes.

truthfully describes the boson-sampling device.

S-VII. CLASSIFICATION

Quantum algorithms for classification on near-term devices have been explored through a variety of approaches [80], although most results are supported by numerical simulations and not implemented in the lab. This is the case for instance of Ref. [51], where the authors present an ansatz for a variational quantum algorithm that is native to photonics. They study the expressivity of the resulting model through theory and numeric simulations. The circuit is made of two trainable blocks with a data encoding block in the middle. This data encoding block consists of phase shifters. For a k -dimensional data point $\vec{x} = (x_1, \dots, x_k)$, each feature x_i is encoded into the phase of a phase shifter. The two trainable blocks are beamsplitter meshes that implement unitary operations, for instance through the encoding of [81] or [82]. The model is studied within the Fock space, considering input states $|n_1^{\text{in}}, \dots, n_m^{\text{in}}\rangle$ and output states $|n_1^{\text{out}}, \dots, n_m^{\text{out}}\rangle$. The total number of photons is denoted n and the number of modes is denoted m .

The authors of Ref. [51] show that the output of the circuit, i.e. the model, can be expressed as $f_{\theta}(x) = \sum_{\omega} c_{\omega}(\theta, \lambda) e^{i x \omega}$, where the frequencies ω depend on the number of photons n input in the circuit, and the Fourier coefficients $c_{\omega}(\theta, \lambda)$ depend on the measurement parameters λ and the chip parameters θ .

We can see how interesting it is to use a photonic encoding and in particular to exploit the Fock space from the perspective of expressivity: by adding more photons, more terms will be added to the Fourier series and the resulting model will be more expressive, without increasing the complexity of the circuit or the number of modes. However, it is important to note that this is only possible if PNR detectors are available, so that the output state $|n_1^{\text{out}}, \dots, n_m^{\text{out}}\rangle$ can be resolved beyond $n_i^{\text{out}} = 1$.

Taking inspiration from the results of [51], we design an ansatz for the variational quantum classifier on Ascella containing two parameterizable blocks with a data-encoding block in between. We select modes 3 to 7 on Ascella and construct the first parameterized block using 16 of the reconfigurable thermo-optic phase shifters. The data-encoding block follows, where 4 phase shifters acting on modes 4 to 7 encode the 4 features of each IRIS data point. We then implement another parameterized block with 16 phase shifters. The remaining phases on the chip are either set to 0, when we do not wish to add any extra trainable or encoding phases, or to π , when an interferometer needs to be fully reflective so that no photon escapes to the other modes of the chip. Our ansatz is shown in Fig. S10.

We input into the circuit the 3-photon Fock state $|\psi_{\text{in}}\rangle = |001010100000\rangle$ defined over the 12 modes of Ascella: one photon enters modes 3, 5 and 7 of the chip. We observe different output states $|\psi_{\text{out}}\rangle$ depending on the photon counts observed in the detectors. The resulting model takes the form $f_{\theta, \lambda}(x) = \langle \psi_{\text{out}} | \mathcal{U}^{\dagger}(x, \theta) \mathcal{M}(\lambda) \mathcal{U}(x, \theta) | \psi_{\text{in}} \rangle$.

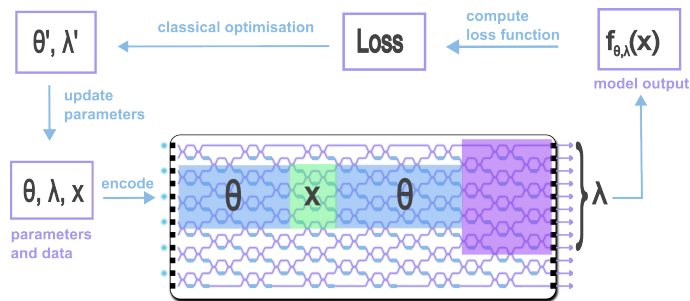


FIG. S10: Representation of our variational quantum classifier on Ascella for the classification algorithm. The trainable blocks parameterized by θ are depicted in blue. The data encoding block is in green. The purple block represents the pseudo-PNR layer, which incorporates four extra modes into the circuit. The model is computed by assigning λ parameters to the outputs at the detectors. All parameters are updated via classical optimization.

The weights λ are assigned to each possible output state observed at the detection step and thus define the observable \mathcal{M} that we are effectively measuring. The operator $\mathcal{U}(x, \theta)$ describes the parameterized and data-encoding blocks. Following the variational approach, we train the model by optimizing classically over the phases θ from the parameterized blocks, as well as over the weights λ .

We demonstrate pseudo photon-number resolution (PNR) partially, on the first and on the last detectors. To this end, we set four phase shifters to $\pi/2$ in the final layer of the chip in order to redirect a portion of the photons from modes 3 and 7 into modes 1, 2 and 8, 9 respectively. We can then reinterpret the detection counts: for instance, observing photons in modes 1, 2 and 3 in our scheme corresponds to observing a three-photon count in mode 3 if we had PNR detectors. Note that implementing this partial pseudo-PNR adds expressivity to our model, as it increases the space of possible outcome states and thus the amount of λ parameters over which we optimize.

For the optimization, we found that performing a see-saw was the most efficient option. This means separating the chip parameters θ from the observable parameters λ into two loops, and finding the best λ for each set of values of θ . The efficiency comes from the fact that tuning one or other set of parameters is not equally costly: changing the θ requires re-configuring the chip, while modifying the λ only involves classical post-processing. We used Gaussian processes to optimize the θ and for each iteration we optimized over the λ using the Nelder-Mead method.

A note about optimizing over the λ parameters: if we were to choose a fixed observable for the variational algorithm and dismiss the λ parameters completely, we may not obtain the same performance for the classifier. Indeed, we would not only have fewer parameters for the optimization but the remaining parameters would be the ones most sensitive to the noise of the experiment. Nevertheless, it is reasonable to grant degrees of freedom to the choice of the observable, so we choose to optimize over the λ as in [51].

In the main text, we summarized the performance of the model using confusion matrices. Fig. S13 shows an alternative display of the results, where the classification estimator is included for each prediction in the dataset along with an error. We evaluated this error knowing that we used 50000 samples for each run of the experiment. Note also that we adapted the definition of the classification estimator of [51] to our case of multi-class classification.

S-VIII. VQE

The Variational Quantum Eigensolver (VQE) [45] for finding ground state energies for a target Hamiltonian can be broken into several steps as follows:

1. Find a Hamiltonian formulation suitable for the problem at hand. To do so, we use the symmetry-conserving Bravyi-Kitaev transformation [47] (available through the *OpenFermion* [48] python package). This provides two very useful pieces of information:
 - The number of qubits necessary to run the VQE.
 - A description of the Hamiltonian in terms of Pauli words which then define coefficients to associate to each measurement basis. We can then construct the expectation value based on this description.
2. Prepare the ansatz. We need a parametrizable circuit expressive enough to be able to reach (a good approximation of) the ground state.

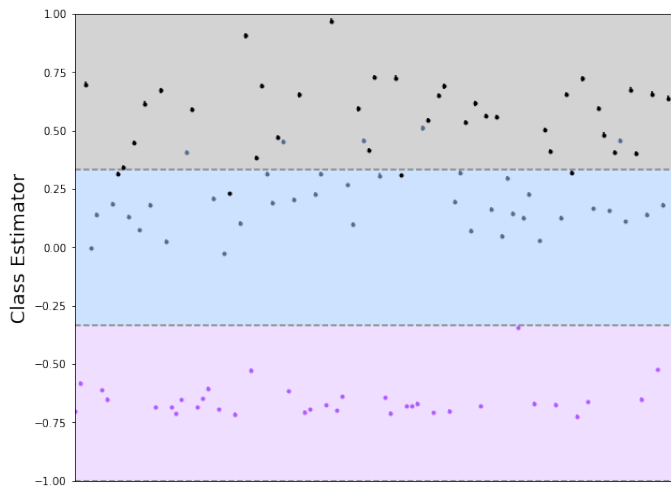


FIG. S11: Training dataset

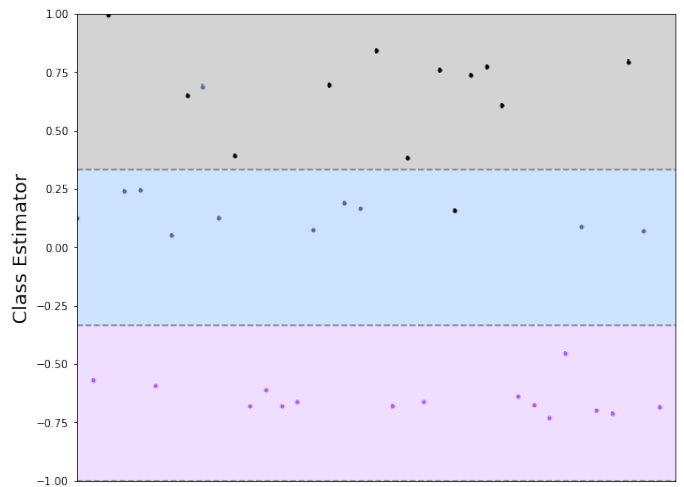


FIG. S12: Test dataset

FIG. S13: Value of the classification estimator, i.e. the model output, displayed for each data point in the train and the test set. The color of the data point indicates its true label while the background color indicates the predicted label. The error bars are obtained via Poissonian statistics from the number of samples used in each run to compute the value of the estimator. The points are simply ordered in the same way as in the dataset.

3. Rotate the ansatz into the basis for each Pauli word operator present in the molecular Hamiltonian, then take a number of samples. Restore the ideal sample counts through error mitigation.
4. Optimize the parameters via a classical procedure (COBYLA algorithm) based on the expectation value computed from the error-mitigated output of the QPU. A classical feedforward loop updates the parameters of the ansatz to reach a lower energy. The evolution of the ground state energy of H_2 with respect to the iterations is represented in Fig. S15.

Hamiltonian description

In order to calculate expectation values of our H_2 Hamiltonian we need to transform the second-quantized version of the Hamiltonian into a qubit basis. This can be done with a number of different transformations such as Jordan-Wigner, but here we use the Symmetry-Conserving Bravyi-Kitaev transform as described in [47, 83]. This involves first reordering the electronic orbitals and then using the Bravyi-Kitaev binary tree mapping. This gives a Hamiltonian which consists of four states that can be assigned in the following way: qubit 1 corresponds to spin-up on the first site, qubit 2 to spin-up on the second site, qubit 3 to spin-down on the first site, and qubit 4 to spin-down on the second site. The Hamiltonian can be further reduced with the symmetries first derived in [84]. There it was noted that the Hamiltonian acts off-diagonally on only two qubits, those indexed 0 and 2. The simulation is begun in the Hartree-Fock state which stabilizes qubits 1 and 3 so that they are never flipped throughout the simulation. This symmetry can be used to reduce the Hamiltonian of interest to the following effective Hamiltonian which acts only on two qubits:

$$\hat{\mathcal{H}}_{\text{qubit}} = \alpha \mathbb{I} \mathbb{I} + \beta Z \mathbb{I} + \gamma \mathbb{I} Z + \delta Z Z + \mu X X \quad (\text{S8})$$

The constants vary with the choice of bond length and can be found in Table S5. The procedure described above is implemented in *OpenFermion* [48]. Thus finding the ground state energy for H_2 for varying bound length can be performed

- with 2 qubits (providing we have an expressive enough ansatz – this is what we tackle in the next subsection),
- by building the expectation values for the measurements ZZ and XX . This is done in a single job on the QPU by tuning the phase shifter in orange in Fig. S14 with micro-increments which allows only a few phases on the Ascella chip to be changed and avoids losing time with full reconfiguration of the chip.

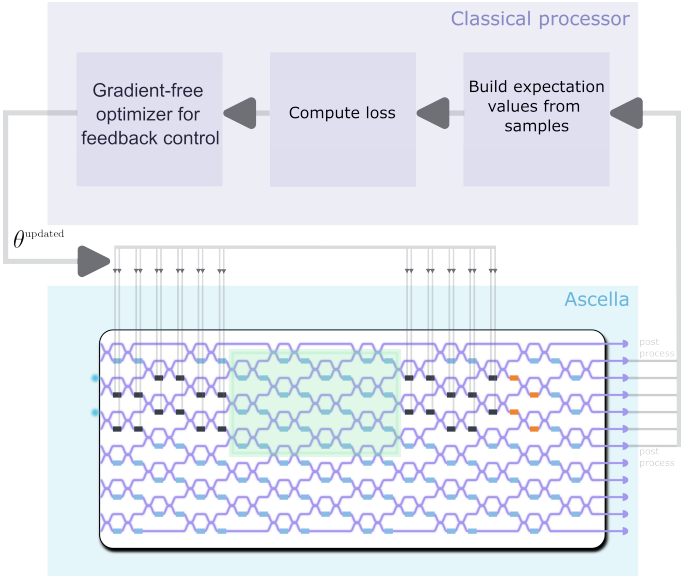


FIG. S14: Procedure for the hybrid photonic VQE algorithm we implement on Ascella. It comprises a QPU block on the bottom that enables the energy of the chosen system to be estimated. The ansatz is parameterized via thermo-electric phase shifters highlighted in black. The green block is a postselected Ralph CNOT [65]. The phase shifter in orange allows selection of the measurement bases required to reconstruct the correct Pauli terms from the qubit Hamiltonian (S8). The outputs from Ascella are fed into a classical block (at the top) which reconstructs the energy. Then it implements a feedback loop back into Ascella via a gradient-free optimizer in order to optimize the angles of the phase shifters to obtain an ansatz closer to the ground state.

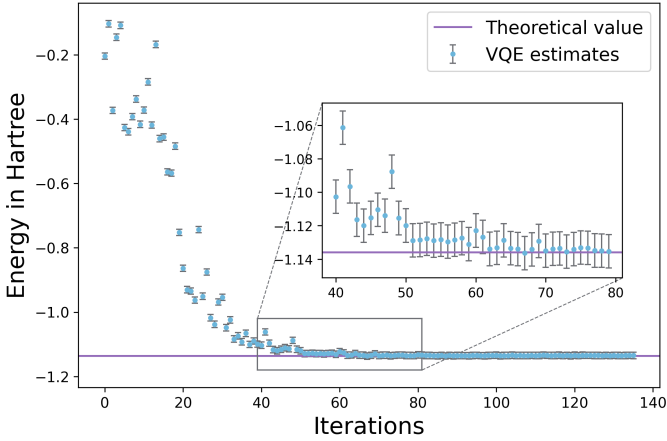


FIG. S15: Evolution of the ground state energy of H_2 obtained by the VQE procedure on Ascella with the number of iterations.

Ansatz preparation

In the present context, the idea behind using the VQE algorithm is to produce a parameterizable ansatz expressive enough to get very close to a 2-qubit ground state of the desired Hamiltonian in order to obtain the ground state energy. The gate-based circuit below (see Fig. S16) can generate any 2-qubit state by Schmidt decomposition (one R_X rotation at the end can be removed in principle since it amounts to removing the global phase).

This wave ansatz can be implemented photonicly. To deal with noise and because using more parameters can be helpful for converging faster to the ground state energy, we use the ansatz represented in Fig. S14 where we path encode the 2 qubits with one photon per pair of modes 2–3 and 4–5 (the first mode being the 0th one). This comprises 20 tunable phase shifters. Modes 1 and 6 are used as ancillary mode for the postselected Ralph CNOT. The CNOT

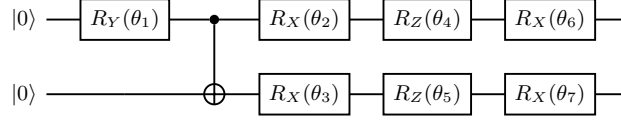


FIG. S16: Gate-based version of an ansatz circuit with 7 parameters controlling 7 parameterized rotations capable of generating any 2-qubit state.

is constructed from our transpilation algorithm. We use parametrizable thermo-electric phase shifter (represented in black on Fig. S14) to control the optical index in the waveguide and thus tune the phase of the photons so that we can achieve any 2-qubit state.

Error Mitigation

We use the quantum error mitigation (QEM) technique proposed in [85] and first experimentally demonstrated in [49] to more consistently converge to the correct ground state energy by mitigating state preparation and measurement (SPAM) errors. The idea is to mitigate the errors arising from noisy evolution due to thermal noise from the heated phase shifters as well as from the error caused by changing the measurement basis. As detailed in the Methods section, we want to compute left-stochastic matrices Γ_b (for each measurement basis b) such that

$$q = \Gamma_b p, \quad (\text{S9})$$

with q the noisy output probability and p the ideal noiseless output probability. In our case, we have two such Γ_b , which corresponds to a measurement basis in Eq. (S8): XX and ZZ (as III , IZ and $Z\text{I}$ can be obtained from ZZ by classical post-processing).

We construct Γ_b experimentally as follows: $(\Gamma_b)_{ij} = |\langle \psi |_i^b | \psi \rangle_j^b|^2$ is the probability of obtaining the i^{th} eigenvector of b $|\psi\rangle_i^b$ when the j^{th} eigenvector $|\psi\rangle_j^b$ is prepared and measurement observable b is performed. For low enough SPAM errors, each Γ_b is a diagonally dominant matrix and we can retrieve the idealized probability distribution by inverting Γ_b in Eq. (S9). From this procedure we get the two desired matrices as:

$$\Gamma_{ZZ} = \begin{bmatrix} 9.99999952e-01 & 3.09568451e-02 & 3.09568451e-02 & 1.54929555e-09 \\ 2.34741773e-08 & 9.38086308e-01 & 1.45337301e-09 & 2.34741773e-08 \\ 2.34741773e-08 & 1.45337301e-09 & 9.38086308e-01 & 2.34741773e-08 \\ 1.54929555e-09 & 3.09568451e-02 & 3.09568451e-02 & 9.99999952e-01 \end{bmatrix} \quad (\text{S10})$$

$$\Gamma_{XX} = \begin{bmatrix} 9.99999951e-01 & 2.47148265e-02 & 2.47148265e-02 & 1.24580719e-09 \\ 2.39578331e-08 & 9.50570344e-01 & 1.18422748e-09 & 2.39578331e-08 \\ 2.39578331e-08 & 1.18422748e-09 & 9.50570344e-01 & 2.39578331e-08 \\ 1.24580731e-09 & 2.47148287e-02 & 2.47148287e-02 & 9.99999951e-01 \end{bmatrix}$$

Note that for the best performance, the Γ_b matrices should be experimentally evaluated immediately prior to the VQE experiment.

When we obtain our error-mitigated measurement probabilities, we can construct an eigenvalue estimate which is sent to the classical optimizer. We can note the difference between the expectation values compared to simulated values with and without error mitigation in Fig. S17 and see a noticeable improvement, particularly as the energy nears the ground state. We note that the simulated and error-mitigated values have a close to perfect agreement. This mainly comes from the correction of the basis rotation gates.

Classical optimization

The classical part of the VQE algorithm is performed on the dark blue classical processing unit (CPU) box in Fig. S14. The expectation values for the terms of $\hat{\mathcal{H}}_{\text{qubit}}$ are constructed from error-mitigated samples from the QPU. Then the loss function $\langle \hat{\mathcal{H}}_{\text{qubit}} \rangle$ is constructed by summing the 5 terms comprising Eq. (1). The CPU calls the COBYLA optimizer to perform a gradient descent and find the new set of angles to feed the QPU. Convergence of the procedure is shown in Fig. S15.

At each step, we compute the energy from 10000 processed samples. This amounts to a 0.013 probability that our sampling error is greater than 0.01 Hartree. It is worth noting here that the optimizer can occasionally converge to

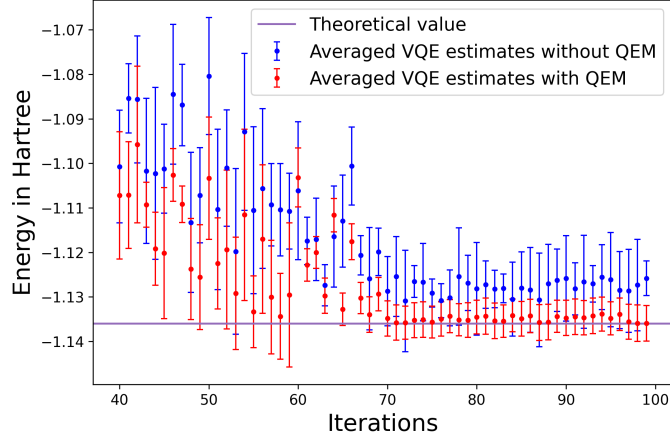


FIG. S17: Comparison with and without SPAM error mitigation by averaging loss values over 45 runs. Error bars are the standard deviation for the average.

Radius (Å)	Hamiltonian Coefficients				
	α (III)	β (ZII)	γ (IIZ)	δ (ZZ)	μ (XX)
0.2	2.0115282039582	0.9304885285175	0.9304885285175	0.013623865138623	0.157972708628
0.25	1.4228278945358	0.8706459577114	0.8706459577114	0.013463487127669	0.15927658478468
0.3	1.0101820841922	0.8086489099089	0.8086489099089	0.013287977089941	0.16081851920392
0.35	1.0101820841922	0.8086489099089	0.8086489099089	0.013287977089941	0.16081851920392
0.4	0.4603634956295	0.688819429564	0.688819429564	0.01291396933589	0.1645154240225
0.45	0.2675472248053	0.6338897827590	0.6338897827590	0.012719203005418	0.16662140112466
0.50	0.11064654485357	0.5830796254889	0.5830796254889	0.01251643158428	0.16887022768973
0.55	-0.0183735206558	0.5364887845888	0.5364887845888	0.012300353656101	0.17124451736495
0.65	-0.2139316272136	0.45543342027862	0.4554334202786	0.011801922101754	0.17631845161020
0.75	-0.3498334175179	0.38874758809160	0.38874758809160	0.011177144762525	0.18177153657730
0.85	-0.4454236322275	0.3337464949796	0.3337464949796	0.01040606826223	0.18756184791877
0.95	-0.5135484185550	0.2877959899385	0.2877959899385	0.009503470221825	0.19365031698524
1.05	-0.5626001130028	0.24878328975518	0.24878328975518	0.008509936866414	0.19998426653596
1.15	-0.5979734705198	0.2152339371429	0.2152339371429	0.007477201225847	0.2064946748241
1.25	-0.6232232011799	0.1861731031999	0.1861731031999	0.006455593489009	0.2131024013141
1.35	-0.6408366121165	0.1609263900897	0.1609263900897	0.005486217221390	0.21972703573593
1.45	-0.6526612024877	0.13897677941251	0.13897677941251	0.004597585574594	0.22629425934361
1.55	-0.6601174612872	0.11989353736336	0.11989353736336	0.0038055776890	0.23274029161766
1.65	-0.6643091838424	0.10330532972950	0.10330532972950	0.003115459300252	0.23901364608341
1.75	-0.6660923101667	0.08889055166239	0.08889055166239	0.00252481503720	0.24507502046287
1.85	-0.6661263822710	0.07637119958665	0.07637119958665	0.002026489193459	0.2508961512677
1.95	-0.6649159578993	0.06550649596835	0.06550649596835	0.001610984321150	0.2564582470193
2.05	-0.6628441004621	0.05608661275595	0.05608661275595	0.001268117568204	0.26175037476834

TABLE S5: List of Hamiltonian coefficients from Eq. (1) for varying bond length.

a local minimum of the objective function, due to the vanishing gradient or barren plateau problem which is avoided in most experiments.

S-IX. GHZ-FACTORY

The layout of the GHZ-factory photonic circuit adapted from Ref. [13, 66] is presented in Fig. S18.

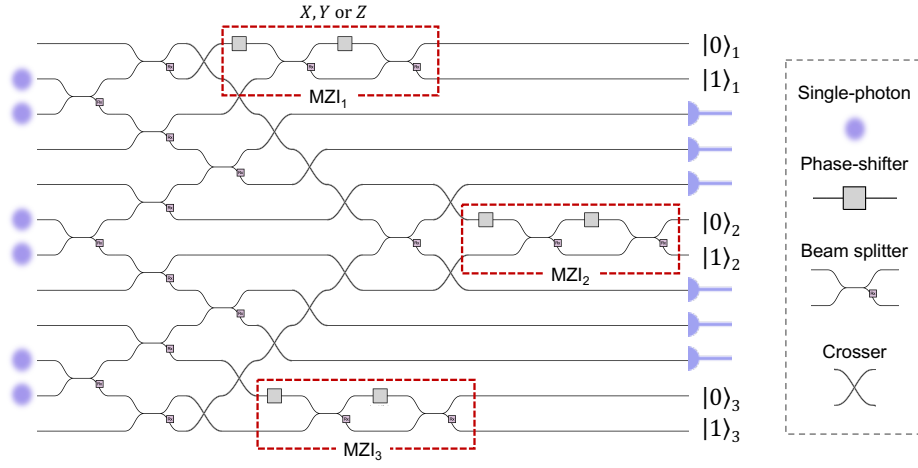


FIG. S18: GHZ-factory photonic circuit from *Perceval*. Six single photons (purple dots) are sent to the input optical modes (2, 3, 6, 7, 10, 11). Three qubits are path encoded in the output optical modes (1, 2), (6, 7) and (11, 12). To account for the losses in the optical system we postselect on the detection of one and only one photon per qubit. We use reconfigurable Mach-Zehnder interferometers to project the generated state in the Pauli matrix basis (\mathbb{I}, X, Y, Z).